Received: 25 May 2022 | Revised: 13 February 2023 | Accepted: 18 March 2023

DOI: 10.1002/met.2125

Meteorological Applications
Science and Technology for Weather and Climate
Open Access
RMetS

RESEARCH ARTICLE

Upper tropospheric cloud-radiation interaction induced by monsoon surge over the South China Sea

Shunya Koseki[1,2] | **Ricardo Fonseca**[3,4] | **Tieh-Yong Koh**[2,4,5] | **Chee-Kiat Teo**[2,4,6]

[1]Geophysical Institute, University of Bergen/Bjerknes Centre for Climate Research, Bergen, Norway

[2]Temasek Laboratories, Nanyang Technological University, Singapore, Singapore

[3]Environmental and Geophysical Sciences (ENGEOS) Labs, Khalifa University, P.O. Box 127788, Abu Dhabi, UAE

[4]Earth Observatory of Singapore, Nanyang Technological University, Singapore, Singapore

[5]College of Lifelong and Experimental Learning, Singapore University of Social Sciences, Singapore, Singapore

[6]Centre for Climate Research Singapore, Meteorological Services Singapore, Singapore, Singapore

Correspondence
Shunya Koseki, Allégate 70, Bergen, 5007, Norway.
Email: shunya.koseki@uib.no

Abstract

We have investigated cloud formation over the South China Sea in the upper troposphere and its impacts on the radiation budget of the troposphere and ocean surface under monsoon surges using satellite and reanalysis products and an atmospheric numerical model. During strong surges (SS), the upper tropospheric (UT) cloud formation in central South China Sea shows a clear diurnal cycle, peaking around 12–14 local solar time when the incoming solar radiation is the strongest. The enhanced UT clouds attenuate the incoming solar radiation in the upper troposphere reducing the net downward shortwave radiation flux at the surface by approximately 28% in SS compared with no surge case. In contrast the downward longwave radiation flux is enhanced mainly from the middle to upper troposphere in SS. The cooling because of the diminished incoming shortwave radiation overwhelms the warming due to the longwave radiation at the ocean surface. This cloud radiative forcing is observed partly over the cold tongue in sea surface temperature (SST) in the South China Sea. Numerical simulations with a 1-dimensional slab ocean model suggests that the monsoon-induced UT cloud radiative forcing contributes partially to maintain and reinforce the SST cold tongue with a tendency of about 0.08 K in 6 days or about 1/6 of one standard deviation of the Cold Tongue Index in December. The latent heat flux due to the monsoon surge is still the most significant factor maintaining the cold tongue.

KEYWORDS

climate change impacts, energy, extreme rainfall, forecasting, monsoon, topical climates

1 | INTRODUCTION

Clouds play an important role in controlling the global and regional climatological mean state and its multiscale temporal change through radiative interaction and feedback (e.g., Stephens, 2005; Williams et al., 2003). Understanding the impact of cloud radiative forcing on the climate is one of the most important topics to the scientific community and numerous works on the effects of clouds on the radiation have been carried out using satellite-derived data and numerical models (e.g., Charlock & Alberta, 1996; Rossow & Schiller, 1991, 1999). In particular, shortwave and longwave radiation fluxes (LWFs) are significantly modified by clouds, and their interactions with clouds

are largely complicated (e.g., Gu et al., 2011). Such a modification of radiation fluxes due to clouds has been reported ubiquitously over all regions and at all altitudes in the troposphere and stratosphere. In the upper troposphere and lower stratosphere, cirrus clouds form frequently and impact the surface and top of the atmosphere radiative energy budgets (e.g., Liou, 1986). In the lower troposphere, the frequent marine stratus cloud formation is found over the relatively cool ocean surface (e.g., Klein & Hartmann, 1993; Koshiro & Shiotani, 2014; Lauer et al., 2009; Wang et al., 2004) and contributes to the atmospheric boundary layer and ocean mixed layer heat budgets through longwave radiative cooling at the cloud top of the cloud layer (e.g., Huang, Liu, et al., 2011; Huang, Tian, & Steinke, 2011; Koseki et al., 2012) in addition to its effective attenuation of the incoming solar radiation. A better understanding of cloud-radiation interactions and subsequent improved simulation of the surface radiation fluxes will also help to optimize solar power generation (e.g., Miller et al., 2018), an increasingly important energy source on a global scale (e.g., Devabhaktuni et al., 2013).

The Maritime Continent is one of the tropical regions where the upper-level cloud formation is the most frequent (e.g., Eguchi & Shiotani, 2004; Norris, 2005). This is particularly true during the Asian winter monsoon, when monsoon convection travels southward along the South China Sea and Maritime Continent from September to February. Occasionally, the Asian winter monsoon convection is abruptly reinforced by the so-called, monsoon surge events (Chang et al., 2003), which are associated with southward intrusions of colder and drier air from the Asian continent and may induce severe natural disasters such as heavy rainfall and flooding in Southeast Asia (e.g., Hattori et al., 2011; Trilaksono et al., 2012). The enhancement of rainfall is caused by the interaction of the local sea/land breeze circulations with the background monsoonal surge (e.g., Joseph et al., 2008; Koseki et al., 2013; Qian et al., 2010) enhanced by topographic lifting (e.g., Seko et al., 2008). These monsoon surge events are one of the characteristics of the Asian winter monsoon system in the Maritime Continent. Upper tropospheric (UT) cloud formation is induced by moist cumulus convection, which helps transport water vaporvapour upward from the moisture-rich lower troposphere to the dry upper troposphere (e.g., Frederick & Schumacher, 2008; Mace et al., 2006; Zelinka & Hartmann, 2009). UT humidity and cloud formation normally co-occur (e.g., Inai et al., 2012; Kahn et al., 2009; Lamquin et al., 2008; Sandor et al., 2000; Spichtinger et al., 2004; Störm et al., 2003; Udelhofen & Hartmann, 1995; Zelinka & Hartmann, 2009) and consequently, the radiation budget in the troposphere is modulated by the enhanced UT cloud formation. Feng et al. (2011) from the analysis of satellite data concluded that anvil clouds associated with deep cumulus convection give a higher contribution to the total cloud radiative forcing in both of shortwave and longwave compared with cumulus convective clouds and stratus clouds.

An important feature of the South China Sea is the relatively cool ocean surface, the so-called cold tongue (e.g., Huang, Liu, et al., 2011; Huang, Tian, & Steinke, 2011; Liu et al., 2004; Thompson et al., 2016), present in the winter monsoon season. The cold tongue is generated by the monsoon-driven western boundary current along the coast of Vietnam (Liu et al., 2004). On the other hand, recently published work reported that the diurnal cycle of solar radiation accounts for some of the variation in SSTs in the tropics (e.g., Bernie et al., 2005; Shinoda & Hendon, 1998). Therefore, we can expect that the modified cloud formation during monsoon surge events will have some influence on the ocean surface; in particular, the cold tongue will be modified through the radiation budget over the South China Sea. The interaction between clouds and the underlying SSTs is complicated owing to the triggering of cloud formation by the (warm) ocean surface and the subsequent feedback from the clouds on the SSTs through their radiative forcing.

In this study, we aim to clarify how the cloud formation over the South China Sea associated with the winter monsoon surges changes the radiation fields in the troposphere. Furthermore, we examined the impact of cloud radiative forcing on the temperature tendency of the South China Sea ocean surface, particularly on the climatological cold tongue. This paper is structured as follows: Section 2 provides the data set and a summary of the configuration of the numerical model employed in this study. An evaluation of the regional climate model performance is presented in Section 3. The diurnal cycle of cloud formation is given in Section 4 and the radiation budget in the troposphere is discussed in Section 5. A brief estimation of the cloud radiative forcing on the ocean using a simplified slab ocean model is conducted in Section 6. Finally, we summarize the results in Section 7.

2 | DATA, MODELS AND METHODOLOGY

2.1 | Observational/reanalysis data

In this study, we utilized the Climate Forecast System Reanalysis (CFSR) data developed by the National Centers for Environmental Prediction (NCEP) (Saha et al., 2010) covering 1979 to 2010 and the infrared imagery data of the Geostationary Meteorological Satellite (GMS) data managed by the Japanese Meteorological Agency (JMA), which extends from 1995 to 2008. This GMS data covers a

relatively long temporal period (1995–2008) and has a relatively high spatial (5 km) and temporal (1 h) frequency over the target region in the South China Sea. Other satellite datasets such as CloudSat (Stephens et al., 2002) can provide additional variables related to cloud microphysics and vertical cloud distributions but with a much reduced temporal extent, due to the limited observations by the sensors over the same location each day compared with geostationary satellites. What is more, CloudSat was launched in April 2006 and, as noted in the next subsection, there are only 4–5 days for which our model output and CloudSat data are both available, and even for these the overlap is rather limited. Although we recognized that any error in representing the cloud distributions in the model can potentially impact the analysis of radiation, we note that high-frequency temporal data and the high availability of data covering the South China Sea are crucial for cloud formation and radiation forcing studies over the region during monsoon surges. Therefore, we opted for the GMS data for the evaluation of the weather research and forecasting (WRF) simulation with respect to cloud properties for this study. A more in-depth evaluation of the WRF-predicted clouds and their microphysical characteristics with other more advanced satellite observations, such as CloudSat, will be a research project that deserves a full paper and is beyond the scope of this study. Tropical Rainfall Measuring Mission (TRMM; Huffman et al., 2007) version 3B42 and QuikSCAT (Ricciardulli et al., 2011; Ricciardulli & Wentz, 2015) is also utilized from 1998 to 2008 and 1999 to 2006 for precipitation and surface wind respectively, while the SSTs are extracted from the Optimum Interpolated Sea Surface Temperature (OISST; Reynolds et al., 2007) dataset. Further details regarding these datasets are summarized in Table 1.

In this study, monsoon surges are identified based on the daily Cold Surge (CS) Index (Chang et al., 2003), which is defined as the area-averaged horizontal wind speed at 850 hPa within 7.5°–12.5° N and 110°–115° E (black rectangle in Figure 1) of the daily CFSR reanalysis data for the month of December from 1979 to 2010. To highlight the impacts of cumulus convection due to monsoon surges on cloud formation, we classified strong (SS) and no (NS) monsoon surge events with SS (NS), defined as having a CS Index higher (lower) than the climatology plus (minus) one standard deviation of the CS Index. A comparison between SS and NS allows us to highlight the effects of monsoon surge and associated cumulus convection on cloud formation and cloud-radiation

TABLE 1 List and main characteristics of the datasets used in this study.

Datasets	Data type	Spatial resolution	Temporal resolution	Variables considered	References
Climate Forecast System Reanalysis (CFSR)	Reanalysis dataset	0.5° × 0.5° (~55 km) with 37 vertical levels from 1000 to 1 hPa	6-hourly from 1979 to present	Wind; rainfall; outgoing longwave radiation (OLR)	Saha et al. (2010); Freely available online at https://rda.ucar.edu/
Geostationary Meteorological Satellite (GMS) IR1	Satellite	5 km mesh	Hourly from 1995 to 2008	Brightness temperature	Sakurai et al. (2005); https://www.data.jma.go.jp/mscweb/en/index.html
QuikSCAT	Satellite	0.25° × 0.25° (~27 km)	Daily from 1999 to 2006	Surface winds	Ricciardulli et al. (2011); Ricciardulli and Wentz (2015); https://podaac.jpl.nasa.gov/QuikSCAT
Optimum Interpolated Sea Surface Temperature (OISST)	Satellite	0.25° × 0.25° (~27 km)	Daily from 1981 to 2008	Sea surface temperature	Peng et al. (2021); https://www.ncei.noaa.gov/products/optimum-interpolation-sst
Tropical Rainfall Measuring Mission (TRMM) 3B42	Satellite	0.25° × 0.25° (~27 km)	3-hourly from 1998 to 2008	Rainfall	Huffman et al. (2007); https://gpm.nasa.gov/missions/trmm
Weather Research Forecasting (WRF) model version 3.3.1	Numerical Model	18 km (WRF-Nest1) and 6 km (WRF-Nest 2) with 50 vertical levels	Selected 10 years (Table 2)	Wind; temperature; radiation fluxes; OLR; mixing ratio of hydrometeors	Skamarock et al. (2008); https://www2.mmm.ucar.edu/wrf/users/download/get_sources.html

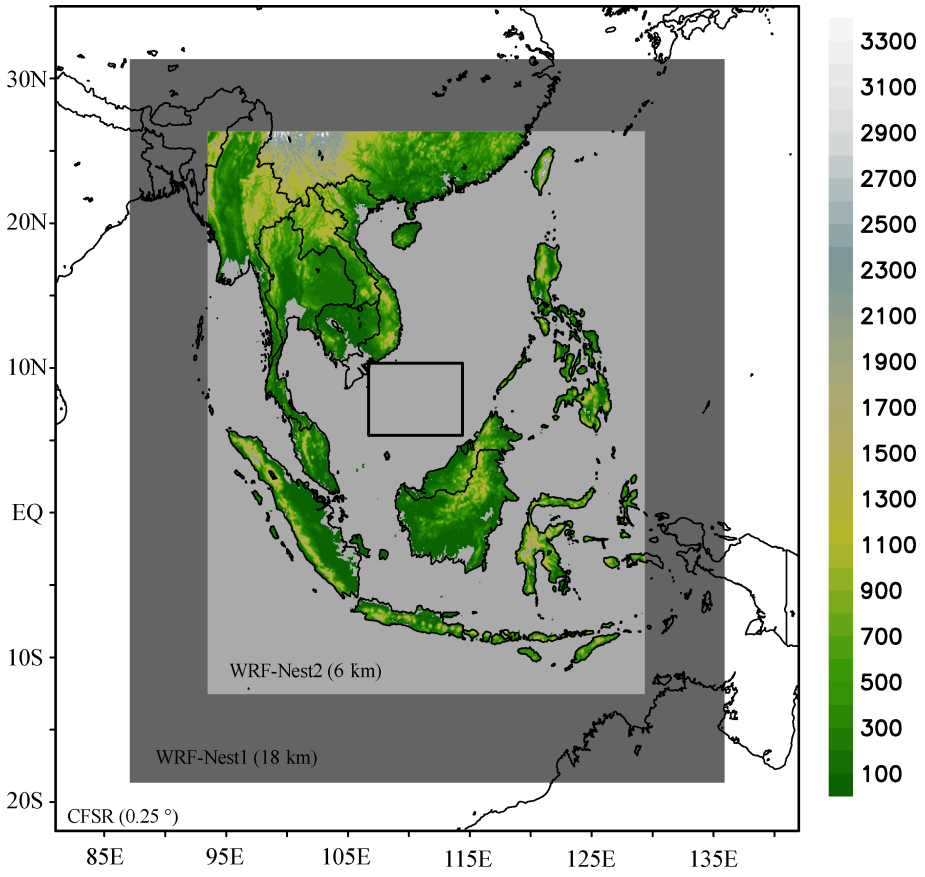

FIGURE 1 The domain for WRF experiments in this study The black box denotes the area for cold surge (CS) Index. Color denotes the terrain height in WRF-Nest2. WRF, weather research and forecasting.

interaction. The number of events for each year is given in Table 2. As this study focuses on general cases of monsoon surge, we exclude the SS events from 9 to 12 December in 1998 and 21 to 26 December in 2001 which are significantly related to the extreme events of tropical cyclone Gil and typhoon Vamei (Aldinger & Stapler, 1998; Chang et al., 2003).

2.2 | WRF model

For further investigation of the UT cloud formation, we employ the Advanced Research Weather Research and Forecasting (ARW-WRF, hereafter, WRF; Skamarock et al., 2008) model version 3.3.1 adopted worldwide for research works on regional weather and climate (e.g., Chotamonsak et al., 2011; Davis et al., 2008; Steele et al., 2013).

We conduct one-way nest experiments using WRF with the model domain shown in Figure 1. The horizontal resolution of the outer grid is set to 18 km × 18 km (WRF-Nest1) and of the inner nest to 6 km × 6 km (WRF-Nest2) with 50 vertical levels in the terrain-following η-coordinate. For analysis purpose, the model output is interpolated to 25 pressure levels. The 16 model η-layers are concentrated between 10 and 16 km with the model top at 30 hPa, for enhanced vertical resolution in the upper troposphere. The topography is interpolated from a 30″ (∼927 m) dataset generated by the US Geological Survey available on the model's website. Given the complex terrain in Southeast Asia (Miettinen et al., 2014), even at 6 km resolution the topography in islands such as Borneo, Sumatra and the Malay Peninsula will not be fully represented by the model. In the top 5 km, Rayleigh damping is applied to the wind components and potential temperature on a timescale of 5 s (Skamarock et al., 2008). Further details regarding the WRF configuration were provided by Skamarock et al. (2008).

WRF-Nest1 is forced by CFSR 6-hourly forecast data (horizontal resolution of 0.5° × 0.5° and 37 pressure levels) with interior analysis (or grid) nudging employed to the horizontal winds, potential temperature perturbation and water vapor mixing ratio above the 800 hPa level and on a time-scale of 1 h. WRF-Nest2 is forced with boundary condition from WRF-Nest1 and run without interior nudging. The output from WRF-Nest1 is discarded. For simplicity hereafter "WRF-Nest2" will be abbreviated as "WRF".

We implement the following physical parameterizations: Betts-Miller-Janjić cumulus scheme specially adapted for the tropics (Fonseca et al., 2016; Janjić, 1994) only for WRF-Nest1, WRF Double-Moment 6-Class cloud microphysics

scheme (Lim & Hong, 2010), Rapid Radiative Transfer Model for GCM longwave and shortwave radiation scheme (Iacono et al., 2008), Unified Noah Land-Surface model (Chen & Dudhia, 2001), Monin-Obukhov surface layer parameterization (Monin & Obukov, 1954), and Yonsei University Planetary Boundary Layer scheme (Hong et al., 2006). A simple prognostic scheme for the sea surface skin temperature that considers the effects of the sensible, latent and radiative fluxes as well as molecular diffusion and turbulent mixing (Zeng & Beljaars, 2005) is also employed.

To reduce computational costs, we sought to simulate only frequent-event years when both SS and NS occurred separately for more than 4 days in December. As shown in Table 2, an analysis of CFSR data revealed 10 years that match the criterion: 1981, 1984, 1985, 1993, 1994, 1995, 1996, 1999, 2000, and 2006. These 10 years are considered for the analyses and model integration. Each integration starts at 00 UTC on November 1st and ends at 00:00 UTC on the following January 1st with the output for December used for this study. We checked and confirmed that the CFSR 6-hourly forecast data providing boundary conditions for our model simulations is in a good agreement with the CFSR-reanalysis in terms of the frequency of SS and NS events and associated cloud formation and hydration in the upper troposphere (not shown).

Although WRF experiments are conducted for the aforementioned 10 years with frequent SS and NS events, we have to recalculate the CS Index and demarcate the modeled SS and NS events for these simulated 10 years as the dates of the SS and NS events. Again to cut down computation costs, we calculate the 10-year climatology and standard deviation of the model's CS Index using only simulations of the December months from 1992 to 2001 (see Table 2). This necessitated conducting only four additional WRF runs for 1992, 1997, 1998, and 2001 (from 00 UTC November 1st to 00 UTC January 1st as before) when either the SS and NS events did not occur frequently enough. Restricting ourselves to a 10-year model climatology and standard deviation only affects the identification of the modeled SS and NS events in the shaded years in Table 2. It does not compromise on the general agreement with the occurrence of these events as represented by the CFSR data. We shall return to this point when examining Figure 3a in Section 3.2.

We present the composite difference between SS and NS for each data set shown in Table 1 to seek a consistent understanding of the impacts of cumulus convection on the higher-level cloud formations. As the available temporal coverage of the satellite datasets is quite short and different from that of CFSR and WRF (see Table 1), it is not appropriate to directly compare its composite results with those from the other datasets. To address this, the composite analysis is conducted in two steps: (1) CFSR composites are taken for the same years as each satellite dataset, referred to as CFSR-S, and (2) CFSR composite is taken for the same years as WRF, referred to as CFSR-W. Each CFSR

TABLE 2 Number of days of strong surge (SS) and no surge (NS) events in December from 1979 to 2010 obtained from Climate Forecast System Reanalysis.

	Strong cold surge	No cold surge
1979	2	4
1980	2	3
1981	9	4
1982	0	2
1983	6	0
1984	10	6
1985	6	9
1986	0	7
1987	3	2
1988	3	4
1989	1	8
1990	7	2
1991	7	0
1992	17	0
1993	7	8
1994	8	8
1995	7	6
1996	12	5
1997	6	3
1998	2	9
1999	8	4
2000	4	10
2001	0	4
2002	2	8
2003	4	3
2004	3	12
2005	3	14
2006	4	5
2007	6	0
2008	2	2
2009	0	5
2010	2	6

Note: Years shaded in gray comprised frequent SS and NS events, occurring at a frequency in excess of 4 days/month. The double circles highlight the continuous 10 years used to generate statistics for WRF-Nest2.
Abbreviation: WRF, weather research and forecasting.

composite was then compared with the respective satellite data and WRF simulations. In this way we attempt to relate the understanding revealed separately by the satellites and WRF-Nest2 via CFSR indirectly.

2.3 | Simplified 1D slab ocean model

In Section 6, we estimate the extent to which the cloud-modified radiation flux possibly changes the sea surface temperature (SST) in the South China Sea using a simplified one-dimensional (1D) slab ocean model. This model is conceptually identical to a non-dynamical version of an ocean mixing layer model developed by Qu (2001) and considers only surface heat flux exchanges between the ocean surface and the bottom of the atmosphere. We make the following assumptions in the model integration: (i) D, the depth of the ocean mixing layer, is constant; (ii) the SST is representative of the temperature of the depth-fixed slab ocean mixing layer; (iii) any ocean mixing processes occur within the depth of D and are completed within each time step; and (iv) all the heat fluxes are processed within the considered ocean mixing layer (for instance, there is no penetration of shortwave radiation below the ocean mixing layer).

The prognostic equation for the SSTs in the slab ocean model is expressed as,

$$\frac{\partial \mathrm{SST}}{\partial t} \equiv \frac{\mathrm{SST}_t - \mathrm{SST}_{t-1}}{\Delta t} = \left[(1-\lambda)R_s + R_l - \varepsilon\sigma(\mathrm{SST}_{t-1})^4 - \mathrm{LH} - \mathrm{SH}\right]/c_w\rho_w D. \quad (1)$$

The forcing inputs to the ocean model are R_s (downward shortwave radiation flux [SWF]), R_l (downward LWF), LH (upward latent heat flux), and SH (upward sensible heat flux). The third term in the square brackets of Equation (1) denotes the longwave radiative emission from the ocean surface to the atmosphere. All heat fluxes are hourly composites of SS and NS (description given in Section 5). The subscripts t and $t-1$ denote the current and proceeding time steps, respectively. For simplicity, the mixed-layer depth D is set to 60 m, the value estimated by Chen et al. (2003) for the South China Sea. The other model parameters are listed in Table 3. The initial condition is the SST December climatology obtained from the OISST data set from the National Oceanic and Atmospheric Administration (NOAA) for the period 1981–2008. The model domain is 0°–15° N and 102°–120° E and the horizontal resolution is 0.25° × 0.25°, equal to that of the OISST data.

TABLE 3 Constants for 1D slab ocean model.

Δt	Time step	3600 s
D	Depth of ocean mized layer	60 m
λ	Albedo of ocean surface	0.07
ε	Emissivity of ocean surface	0.97
σ	Stefan-Boltzman constant	5.678×10^{-8} W m^{-2} K^{-4}
c_w	Isobaric specific heat of sea water	4200 J kg^{-1} K^{-1}
ρ_w	Density of sea water	1000 kg m^{-3}

3 | VERIFICATION OF WRF SIMULATION AROUND SOUTH CHINA SEA

In this section, we look at the UT cloud- and hydro-meteorological fields associated with monsoon surge events over the South China Sea using re-analysis, satellite and WRF data. The inter-comparison is also carried out for model verification purpose.

3.1 | Monthly climatology

Figure 2 summarizes the 10-year (1992–2001) December climatology for CFSR and WRF. The general distribution of the horizontal wind in the lower troposphere simulated by WRF is similar to that of CFSR except mainly for the stronger low-level wind in the model around central Sumatra, the Strait of Karimata (3°–0° S and 105°–110° E) and in northern Borneo (2°–6° N and 113–117° E) which arise because of the high terrain (>1500 m) along the west coast of Sumatra and in northeast Borneo is under-presented even in WRF, as noted in Section 2.2. Intense precipitation is found over the central South China Sea in both the CFSR and WRF, even though the precipitation maximum in the WRF is closer to that of Borneo. Another rainfall maxima are detected in the eastern coast of Malay Peninsula and southwestern coast of Sumatra in both CFSR and WRF. By and large, WRF tends to overestimate the precipitation over the ocean compared with CFSR. These can be attributed to (i) the topography resolution in the model, (ii) its impact on the wind flow (e.g., over Sumatra), and (iii) differences in the cloud microphysics and land surface model schemes.

Outgoing longwave radiation (OLR), a proxy for cloud top height, reflects the deep convective cumulus distribution, particularly on the western coast of Sumatra and the Malay Peninsula in the CFSR. The OLR is smaller over the South China Sea (5°–10° N and 105°–110° E) than its environs in CFSR, which is consistent with the presence of upper-tropospheric clouds, the nature of which is discussed in

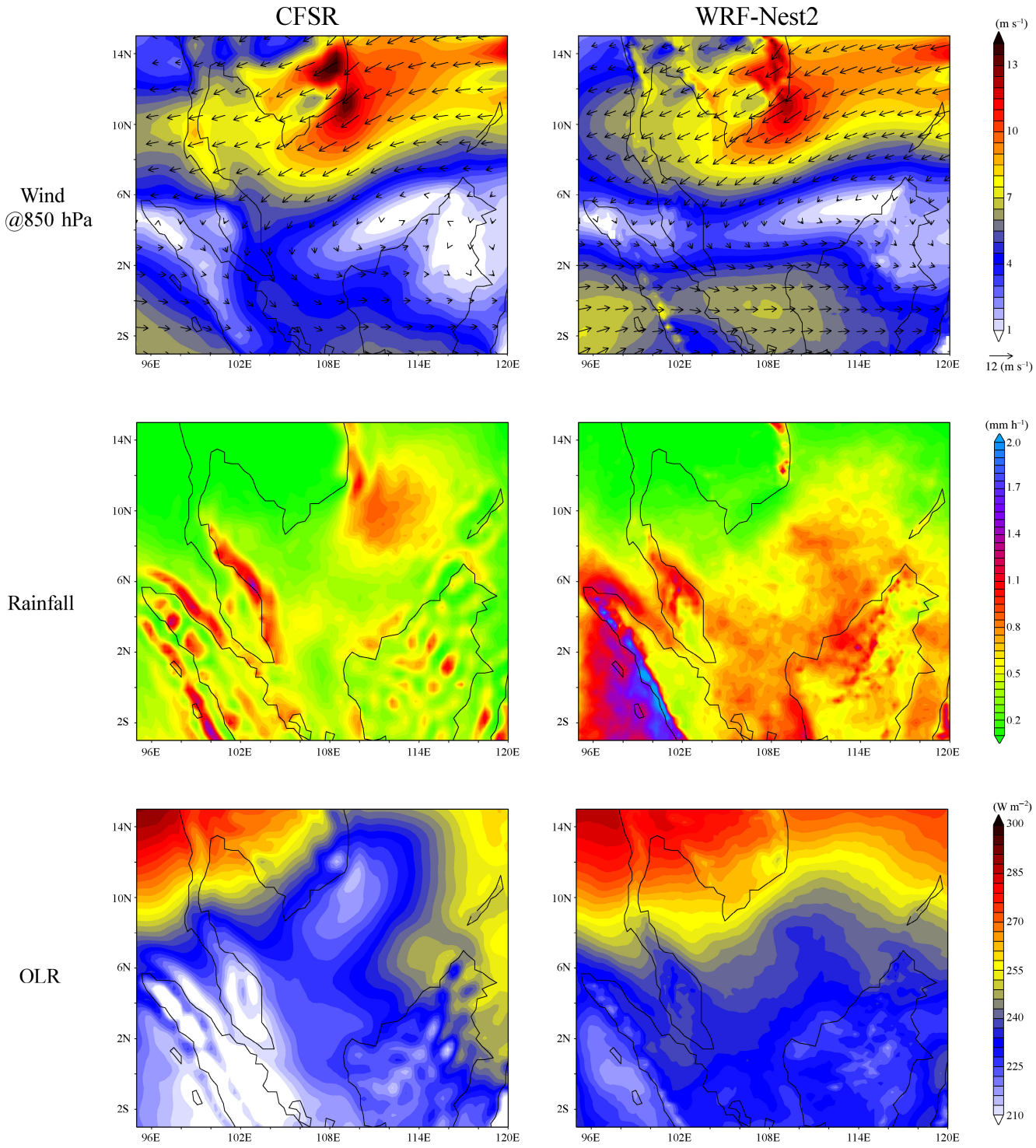

FIGURE 2 Ten-year (1992–2001) climatology of (left) Climate Forecast System Reanalysis and (right) weather research and forecasting for the 850 hPa wind (top; m s^{-1}), the rainfall rate (middle; mm h^{-1}), and outgoing longwave radiation (bottom; W m^{-2}).

Section 4.2. This feature can also be detected in the WRF, although its value is slightly higher than that of the reanalysis dataset. The lower OLR shows a good consistency with higher upper tropospheric moisture in both CFSR and WRF (not shown). A comparison between CFSR and WRF with satellite data will be given in the next subsection in terms of the capability to capture the SS/NS events.

3.2 | Monsoon surge events

The CS Index and its statistics for CFSR's 6hourly forecast and WRF are presented in Figure 3a. Note that the composite of satellite data is based on the CS Index of CFSR. In spite of the lack of data assimilation and interior nudging (for WRF-Nest2), WRF is capable of capturing the

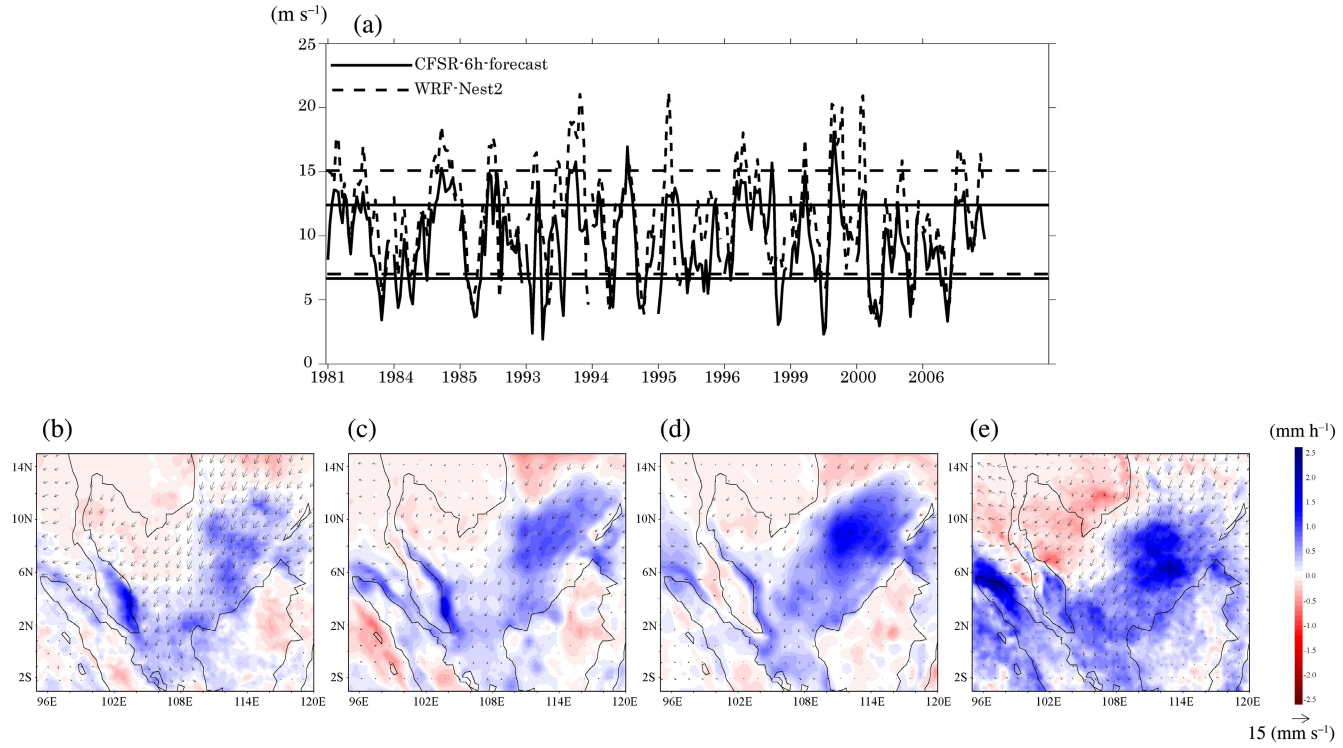

FIGURE 3 (a) CS index obtained from CFSR (solid line) and WRF (dashed line) for the 10 frequent-event years listed in Table 2. Note that the indices from 1 year are not connected to those of the next. The solid (dashed) straight lines denote climatology $\pm \sigma$ of the CS index for CFSR (WRF). (b–e) precipitation (color) and surface wind (vectors) differences between SS and NS for the TRMM/QuickScat, CFSR-S, CFSR-W and WRF, respectively. CFSR, Climate Forecast System Reanalysis; CS, cold surge; NS, no surge; SS, strong surge; TRMM, Tropical Rainfall Measuring Mission; WRF, weather research forecasting.

majority of the SS and NS events for the 10 frequent-event years. The larger standard deviation of the CS Index in WRF is mainly due to the SS events being stronger than in CFSR. The total number of events in WRF is 61 (46) days for SS (NS), whereas CFSR has 74 (61) days for SS (NS) events shown in Table 2.

As seen in Figure 3b, the rainfall of TRMM and CFSR-S is enhanced particularly over the eastern coast of the Malay Peninsula, the northwestern coast of Borneo and the central South China Sea during SS in line with Koseki et al. (2014) and Paunas and Shanas (2017). On the other hand, the rainfall is reduced over the northern South China Sea (12°–15° N and 110°–120° E) and Borneo Inland during SS. CFSR-W and in particular WRF, show a more vigorous rainfall difference than TRMM and CFSR-S, even though the location of where the rainfall is enhanced approximately the same. The positive rainfall bias in WRF as noted in Section 3.1 is seen in Figure 3b. The heavier rainfall in CFSR-W compared with CFSR-S reflects the stronger monsoon surge events in the period considered in the former dataset. Generally, our composite analysis suggests that cumulus convection is enhanced leading to more rainfall in the above-mentioned regions under SS and the converse under NS.

4 | EVALUATION OF MONSOON-SURGE-INDUCED CLOUD FORMATION

4.1 | Daily mean fields

In this section, we compare how cloud formation in the troposphere differs between SS and NS over the South China Sea based on composite analysis. We carried out a two-step composite analysis for precipitation, as described in the previous section. Satellite-derived brightness temperature and model- and reanalysis-estimated OLR are used as proxy indicators for upper-level clouds.

As the cumulus convection and rainfall activities are mainly over the southern part of the South China Sea in the difference between SS and NS (Figure 3b–e), we look for the occurrence of UT clouds in the region between 0° and 15° N. In Figure 4 both cooler T_B and lower OLR indicate that high-level or deep cloud formation is more frequent. Although the two variables cannot be compared quantitatively, we can perform a qualitative comparison assessment. A cool anomaly of T_B is detected over the

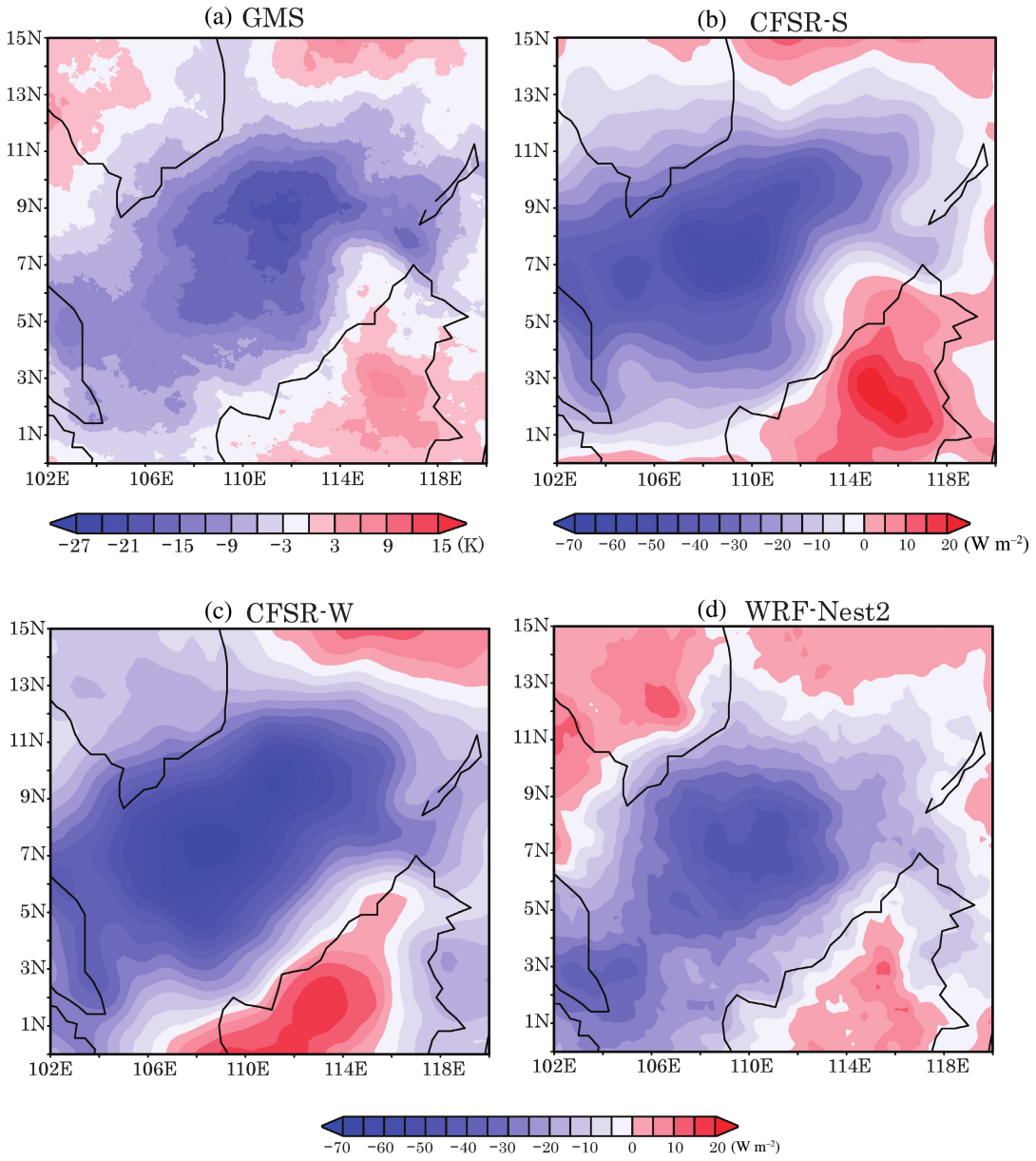

FIGURE 4 Composite difference of (a) brightness temperature of GMS (K) and OLR of (b) CFSR-S, (c) CFSR-W and (d) WRF (W m^{-2}) between SS and NS days. CFSR, Climate Forecast System Reanalysis; GMS, Geostationary Meteorological Satellite; NS, no surge; OLR, outgoing longwave radiation; SS, strong surge; WRF, weather research forecasting.

central South China Sea (5°–11° N and 108°–111° E) and the minimum T_B region is located westward of the most intense rainfall region over the South China Sea. Conversely, the warm anomaly is found over Borneo and the northern part of the domain (13° N ∼ 15° N). CFSR-S shows a similar negative OLR anomaly, with a clear contrast between the South China Sea and the Borneo/northern part of the domain. The WRF OLR shows a good agreement with that of CFSR-W OLR but its magnitude is generally smaller with an OLR anomaly of the opposite sign with respect to that of CFSR-W over much of the Indo-China Peninsula. The differences between CFSR and WRF in Figure 4 are similar to those highlighted in Figure 2. This is because high or deep cloud occurrence is a positive definite variable so that the climatological positive OLR bias (i.e., insufficient cloud) occurs mainly during SS rather than NS events. Such a bias is also evident in the SS minus NS composite and is possibly the result of a weaker radiative feedback (Wang et al., 2015). In any case, the results in Figure 4 confirm that the UT clouds form efficiently under the condition of the strong monsoon surges over the central South China Sea with WRF being capable of reproducing the enhancement of the UT cloud formation over southern South China Sea under strong monsoon surges.

4.2 | Diurnal cycle

To evaluate the results of the WRF-simulated diurnal cycle of the OLR indirectly, we compared it with the brightness temperature obtained from the GMS imagery in Figure 5. CFSR is not adequate for this evaluation because of its coarse temporal resolution (6-hourly). A clear diurnal cycle in brightness temperature can be detected in GMS data: from 01 to 04 LST (LST stands for Local Standard Time, given by UTC + 8 h), the upper-level cloud formation is frequent around the northwestern coast of Borneo and Borneo Inland. The contrast of cloudier and clearer skies becomes remarkable between the sea and land from 07 to 13 LST. In particular, the upper-level cloud formation is most frequent over the central South China Sea between 10 and 13 LST when the incoming solar radiation is the strongest. After this peak, the upper-level cloud decreased gradually over the South China Sea, and the upper-level cloud increased over Borneo from 16 to 22 LST possibly due to increased convection over the land regions (a weaker signal is seen in the Malay Peninsula). Although a quantitative comparison between GMS and WRF is not possible, the model is able to capture the diurnal cycle and the associated land-sea distribution of upper-level cloud formation represented by OLR.

Figure 6a shows the difference of the diurnal amplitude of WRF-simulated OLR between SS and NS. Here, the diurnal amplitude of OLR is defined as the maximum OLR (MAX_{OLR}) − minimum OLR (MIN_{OLR}) at each grid box. A remarkable difference in the diurnal amplitude of OLR between SS and NS events is found over the central South China Sea and northwestern coast of Borneo, where the difference in the daily mean of OLR is the largest as seen in Figure 4d. This suggests that the diurnal variation in upper-level cloud formation is well manifested and more amplified over the South China Sea during SS events.

Figure 6b illustrates the local time of MIN_{OLR} in SS events. Over the central South China Sea, upper-level cloud formation appears to propagate offshore from the inland mountainous region of Borneo (18–20 LST, early evening) to the coastal region (02–04 LST, early morning) and then to the central South China Sea (12–18 LST, afternoon). The average rainfall during SS events over the central South China Sea (black rectangle in Figure 6a), given in Figure 6c, shows the obvious diurnal cycle with the maximum (minimum) between 07 and 09 LST (19 and 21 LST). The OLR time-series also shows a clear diurnal cycle: the minimum (indicating more frequent, taller cloud formation) is around 14 LST and the maximum is around 00 LST. That is, the diurnal cycle of rainfall leads that of OLR by approximately 5–7 h, indicating that the UT clouds investigated here are not associated with the towering cumulonimbus associated with deep moist convection, and are instead likely to be anvil-type clouds formed as remnants of deep moist convection. This time lag between the rainfall peak and the upper-level cloud formation peak is consistent with a shift in the aggregation of the largest rising motion from the lower troposphere (where most surface rainfall is generated) to the upper troposphere (where the lowest brightness temperature is detected) during convective events in line with previous observational studies such as Frederick and Schumacher (2008) and Zelinka and Hartmann (2009).

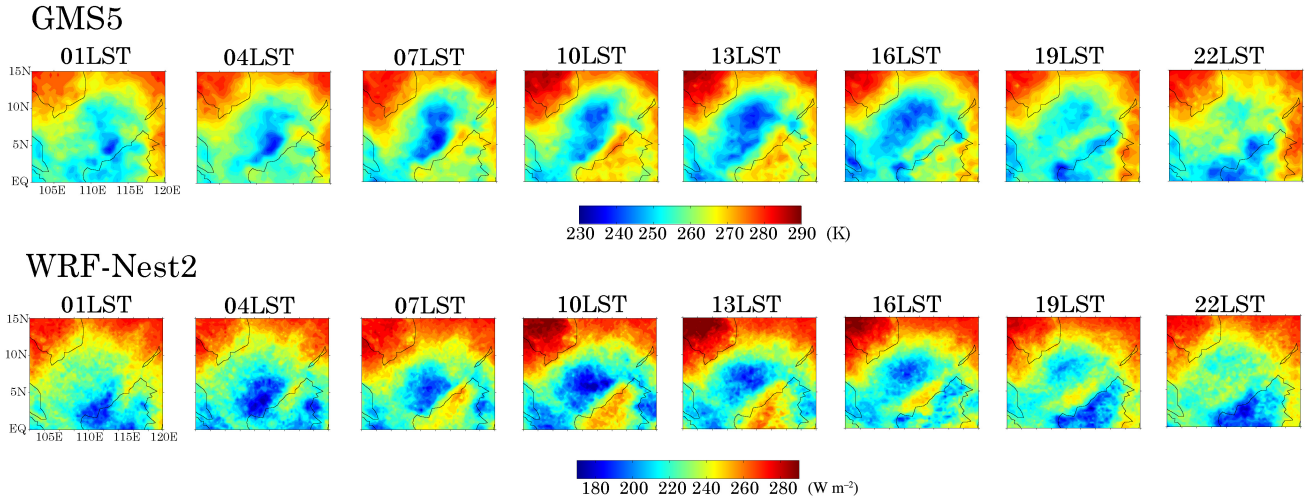

FIGURE 5 3-hourly variability of (top) brightness temperature (K) from Geostationary Meteorological Satellite and (bottom) outgoing longwave radiation (W m^{-2}) from weather research forecasting for a composite of all SS days.

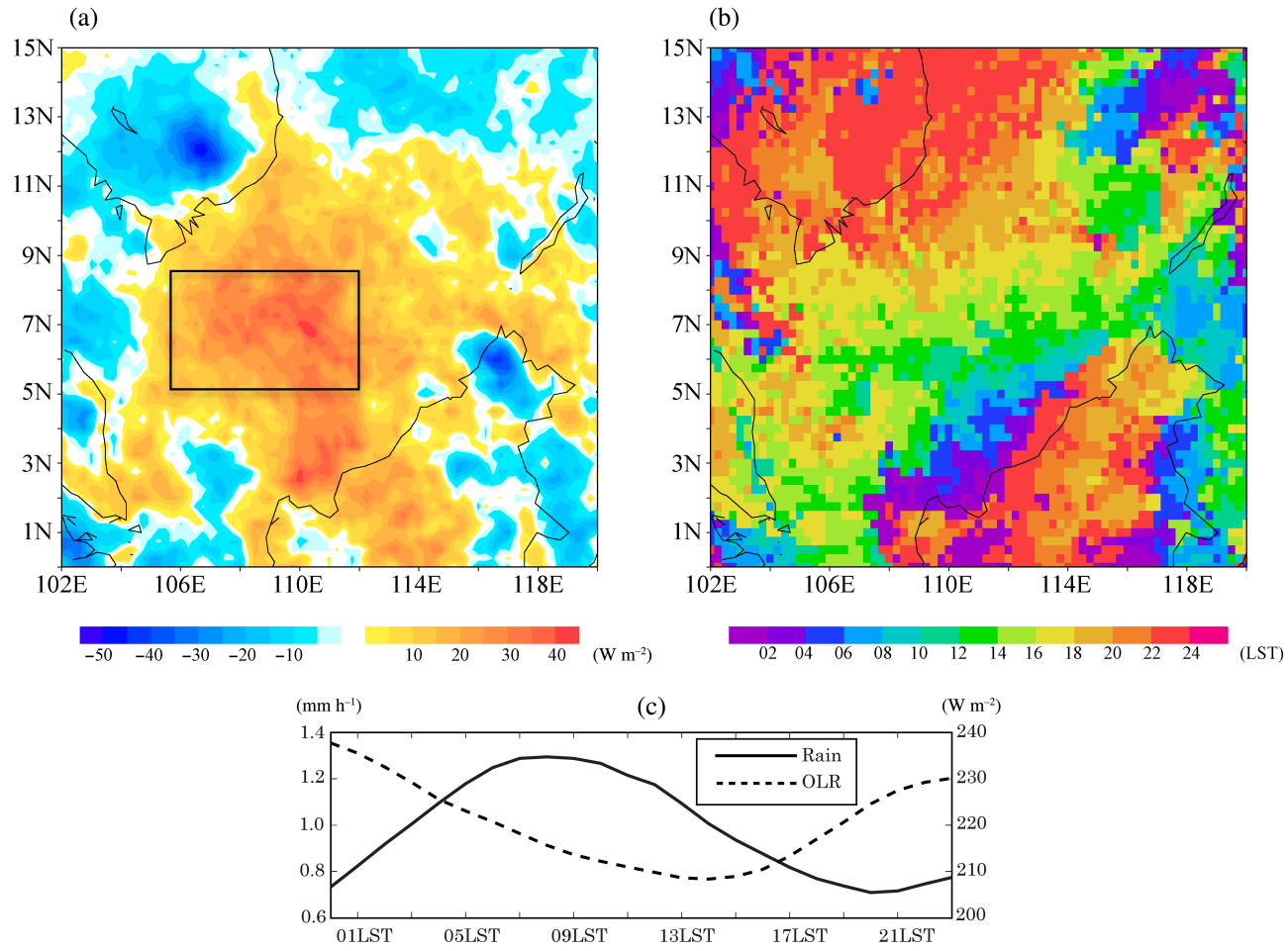

FIGURE 6 (a) Difference in the diurnal outgoing longwave radiation (OLR) amplitude (W m^{-2}) between strong surge (SS) and no surge days and (b) local time of minimum of OLR in SS days from weather research forecasting. In (a) and (b) the model data is binned into a 0.25° × 0.25° grid. (c) Rainfall rate (solid line; mm h^{-1}) and OLR (dashed line; W m^{-2}) averaged over the black box of (a).

5 | ANALYSIS OF THE RADIATION BUDGET

The previous section has shown that strong monsoon surges enhance cloud formation in the troposphere over the central South China Sea. In particular, the UT cloud formation is induced by cumulus convection and has a clear diurnal cycle with a maximum around 13 LST when the solar radiation is the strongest and a minimum around 00 LST. It is anticipated that the radiation budget in the troposphere will be modulated by the frequent cloud formation. In this section, we investigate the tropospheric radiation budget between SS and NS events.

Figure 7 shows the difference (SS minus NS) in the surface daily-mean downward LWF and SWF from WRF. As seen the LWF is slightly positive (∼10 W m^{-2}) over the central South China Sea (4°–10° N and 108°–115° E), where the UT cloud formation is frequent (cf. Figure 7). This enhanced surface-warming effect due to the LWF seems to be associated with the warming effect of the UT clouds that absorb and re-emit some of the longwave radiation preventing it from escaping into space. However, the difference in SWF shows largely negative values (∼−100 W m^{-2}) with a wide-spreading patch over the South China Sea in Figure 9b. The location of this negative SWF is consistent with that of the enhanced UT cloud formation rather than the intense rainfall as seen in Figures 3c and 4d. As the UT cloud formation is at a maximum between 10 and 13 LST over the central South China Sea, as seen in Figure 5, its influence on the incoming solar radiation is optimal. At the surface, the net radiative forcing anomaly over the central South China Sea is negative, that is, the cloud formation due to strong monsoon surges and associated cumulus convection tends to suppress the radiative heating over the central South China Sea (not shown). It is worth noting that the suppressed downward SWF overlaps partly with the cold tongue (Figure 7b). The cold tongue is an oceanic feature of the South China Sea in the boreal winter monsoon season (e.g., Liu et al., 2004; Thompson et al., 2016)

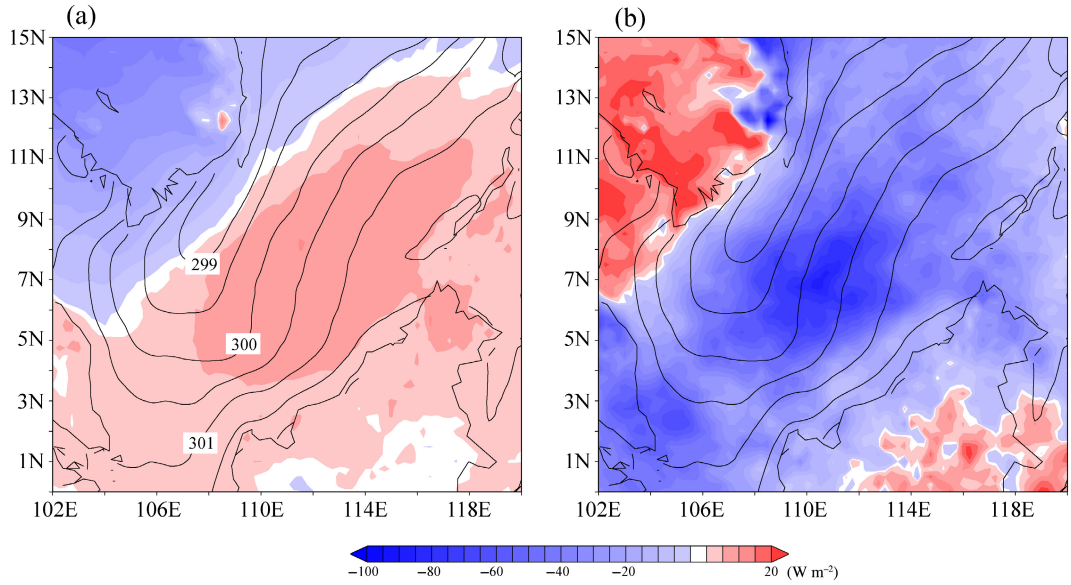

FIGURE 7 Composite difference of the surface (a) longwave and (b) shortwave radiation flux (W m^{-2}) between strong surge and no surge days from weather research forecasting. The solid contours give the 1982–2010 sea surface temperature December climatology, with a contour interval of 0.5 K.

and has some impacts on the regional climate of the Maritime Continent (Koseki et al., 2013; Varikoden et al., 2010). An estimate of how the modified surface radiation fluxes influence the ocean surface temperature will be investigated in Section 6.

As the downward radiation flux at the surface results from the interaction of radiation with clouds and the atmosphere, there is a need to investigate how and where the radiation flux is modulated in the troposphere, as shown in Figure 8. Figure 8a,b shows the results for the downward SWF and LWF, whereas Figure 8c,d the results for the upward SWF and LWF. While the total-sky downward SWF and LWF do not change from the model top down to 100 hPa, the downward LWF (SWF) begins to increase (decrease) around 200 hPa in both SS and NS (Figure 8a). However, the amplification (reduction) rate of LWF (SWF) is much larger in SS than in NS. The difference in downward LWF between SS and NS is the largest between 300 and 400 hPa. The difference in the downward SWF reached a maximum around 500 hPa and did not change much below that level to the surface. The cloud-forcing in terms of LWF and SWF (defined as $F_{CLD} = F_{TOT} - F_{CLR}$, subscripts denote cloud-forcing, total sky, and clear sky, respectively with F representing each radiation flux) show a much clearer difference between SS and NS in Figure 8b. Whereas both the cloud-forcing downward LWF (warming) and SWF (cooling) in NS are small, in SS they are considerable: the downward SWF is reduced by about 90 W m^{-2} between 170 and 500 hPa indicating the attenuation of UT-cloud. The presence of UT-clouds can be seen in Figure 8e (note $\log_{10}$-scale), which shows the area-averaged cloud ice mixing ratio for SS and NS. The cloud ice in SS has the orders of 10^{-5} to 10^{-6}, roughly two to three orders of magnitude much higher than in NS between 200 and 500 hPa, in line with the changes in the radiative fluxes presented in Figure 8a–d. In addition to the cloud ice, other solid-phase hydrolometors like snow and graupel are also intensively generated in SS at the upper troposphere (not shown), and are also likely to influence the cloud-forcing radiation flux. In addition, the cloud-forcing downward SWF is also diminished by about 10 W m^{-2} again between 800 and 900 hPa, suggesting the presence of low-level clouds, with the reduction rate slightly larger in SS than NS, consistent with the higher cloud cover in SS events as evidenced by the high mixing ratio of cloud liquid water in Figure 8e. The downward cloud-forcing LWF in SS has a positive tendency with a maximum between 300 hPa and 400 hPa indicating that the UT clouds absorb the upward LWF from below and re-emit much of it back towards the surface. The slight increase in downward LWF between 800 and 900 hPa is expected due to the likely occurrence of low-level clouds as suggested by the decrease in downward SWF.

The results for the upward LWF and SWF are now considered (Figure 8c,d). While the upward total-sky LWF is diminished from the surface to the upper troposphere in both SS and NS, its rate of decrease is larger in SS. The SWF in SS and NS increases drastically between 500 and 200 hPa and modestly between the surface and 800 hPa where the downward SWF is attenuated in Figure 8a,b. As seen in Figure 8d, the cloud-forcing

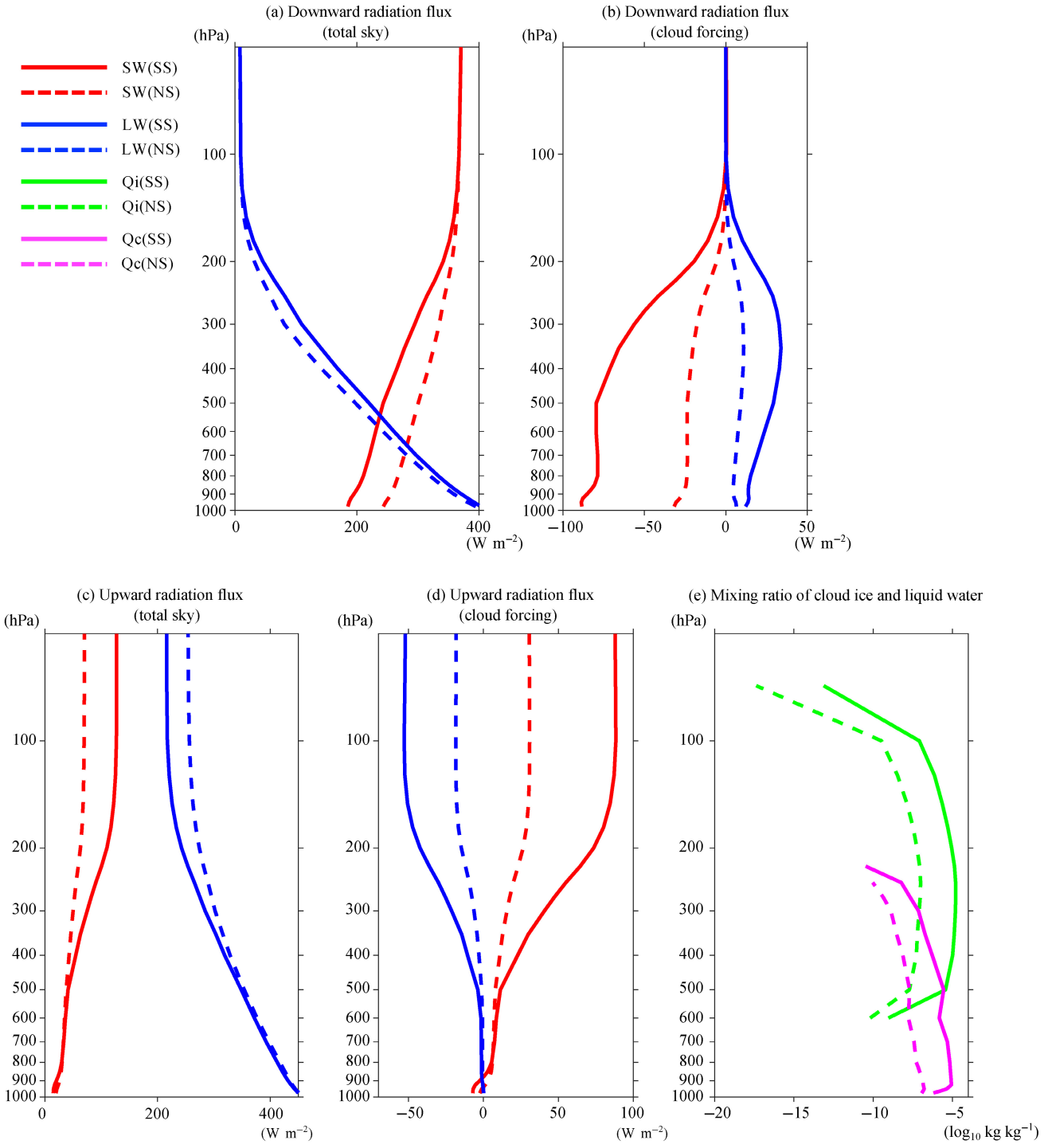

FIGURE 8 Vertical profile of downward (a) total-sky and (b) cloud forcing radiation fluxes (W m^{-2}) averaged over the black box in Figure 6a for strong surge (SS) (solid line) and no surge (NS) (dashed line) days. (c) and (d) are as (a) and (b) but for the upward fluxes. The fluxes due to cloud forcing given in panels (b) and (d) are estimated by taking the difference between the total sky and the clear sky radiation fluxes. (e) Vertical profile of log-scaled mixing ratio of cloud ice (Qi, green) and cloud liquid water (Qc, magenta) averaged over the black box in Figure 6a for SS (solid) and NS (dashed).

upward LWF in SS is negative and much more negative than that in NS, indicating that the loss of LWF from the atmosphere to space is more efficient in NS as the UT clouds tend to absorb the upward LWF and re-emit less upward. As shown in Figure 8c, the upward cloud-forcing SWF in SS increased significantly between 500 and 200 hPa, whereas the rate of increase in NS was smaller, as shown in Figure 8d. This implies that the

solar radiation is reflected by the UT clouds, which are anvil-type clouds and therefore thicker than cirrus clouds, that are more frequent in SS. This reflection of the solar radiation can be also detected in the lower troposphere between 800 and 900 hPa in SS as a results of the likely presence of low-level clouds (Figure S1). Thus, the enhanced UT cloud formation tends to cool the atmosphere in terms of the SWF, as is also suggested in Figure 8b. We have compared the clear-sky SWF and LWF between SS and NS events and found that there is little difference in the vertical profiles (not shown).

The thick concentrated ice and mixed-phase clouds in the upper troposphere dominate the influence on the radiative fluxes, while low-level water clouds have just discernible influence (not shown). According to Feng et al. (2011) and Wall et al. (2018), cloud radiative forcing in cumulus convection is largely contributed by anvil-type clouds because of their wide coverage area. Therefore, the enhanced UT cloud modeled by WRF likely represents anvil-type clouds rather than cumulus or cirrus clouds in the real world. Further insight on the nature of the UT clouds can be gained by analyzing satellite observational data products such as CloudSat (Stephens et al., 2002) and considering a new set of SS and NS events for which both model and satellite data are available.

6 | RADIATIVE FORCING ON THE OCEAN SURFACE

Section 5 showed that the reduced SWF at the surface partially overlaps with the cold tongue over the central South China Sea (Figure 7). In this section, we explore how the modified cloud radiative forcing due to monsoon surges impacts SSTs in the central South China Sea using a simplified 1-dimensional (1D) slab ocean model. While a 1D model does not permit horizontal advection, it has been shown that one of main mechanisms for maintaining the cold tongue is through surface evaporation (e.g., Thompson et al., 2016). Our interest here is to clarify the relative importance of the surface radiation against surface evaporation in the maintenance of the cold tongue.

6.1 | Series of experiments

We integrate the slab-ocean model described in Section 2.3 forced by hourly composites of the surface heat and radiation fluxes (downward shortwave radiation, downward longwave radiation, latent heat and sensible heat) in SS as a benchmark (hereafter referred to "full flux", FL) of sequential experiments. We conduct sensitivity experiments (hereafter referred to by their labels in parentheses) in which the hourly (1) surface downward SWF (SWO), (2) surface downward LWF (LWO), (3) latent heat flux (LHO), (4) sensible heat flux (SHO), and (5) all of the above fluxes (AO) are swapped with the correspondent NS composite values. All experiments are integrated under the repeated diurnal cycle forcing for 6 days using the December SST climatology of OISST from 1981 to 2008 as initial condition. Six days are chosen because it is the secondary maximum in the frequency histogram of the duration of SS events and accounts for the highest number of days of SS (Figure 9a). We made another assessment of the December-mean latent heat flux in the South China Sea with a blended satellite-derived and modeling product (not shown). Although the WRF simulation tended to overestimate the evaporation in the South China Sea by up to 50 W m^{-2}, its spatial pattern is well captured by the model. The overestimation in the magnitude of the latent heat flux is attributed the prescribed SSTs used in the simulation which prevent air–sea interaction from taking place. As the air–sea interaction is very active in the South China Sea during the boreal winter monsoon season (Koseki et al., 2013), a coupled simulation would be desirable for more a realistic investigation of the monsoon surge-SST interaction in the South China Sea.

Figure 9b,c shows Hovmöller diagrams of hourly downward SWF and LWF at the surface for NS (solid contours) and the difference between SS and NS (shading) averaged between 4° N and 8° N. As the top-of-atmosphere downward SWF is most intense around local noon coinciding with frequent UT cloud formation in SS (Figures 6 and 7), the reduction of the incoming solar radiation is more drastic in SS than in NS (by ∼−220 W m^{-2} at 12 LST over the central South China Sea as seen in Figure 10b). Whereas the downward LWF at the surface is enhanced by UT clouds in SS, the enhancement is not more than 10 W m^{-2} over the South China Sea (Figure 9c). Compared with the SWF, the latent and sensible heat fluxes do not exhibit obvious diurnal variations over the sea. However, these heat fluxes are much larger in SS than in NS because of the stronger surface wind, 193.94/83.81 W m^{-2} for the latent heat flux and 13.91/5.77 W m^{-2} for the sensible heat flux in SS/NS events, respectively.

6.2 | Results

We compare the SSTs after 6 days in the five sensitivity experiments (AO, SWO, LWO, LHO, and SHO) against the benchmark experiment (FL) in Figure 10. The SST difference between AO and FL indicates the comprehensive

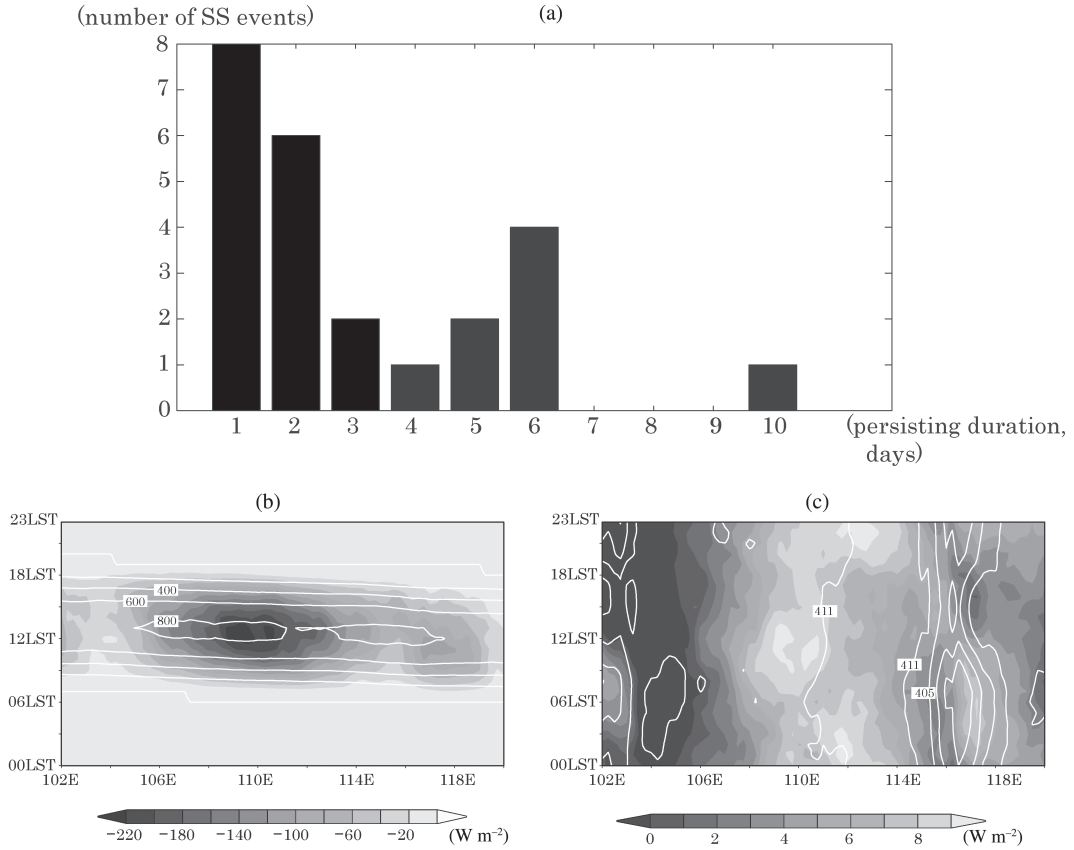

FIGURE 9 (a) Frequency of persistence (day) of strong surge (SS) events. (b) and (c) give the difference (SS minus no surge [NS]) in hourly composite downward shortwave and longwave radiation flux (W m^{-2}) at the surface, respectively, in shading. The white contours in these panels denote the hourly composite of each flux for NS days (W m^{-2}). Both panels show area-averaged fields between 4° N and 8° N.

thermal impacts of the strong monsoon surge on the ocean surface as the SST becomes much cooler (∼−0.5 K/6 days) over the whole South China Sea (Figure 10a). In particular, the core of the cold tongue is intensified and broadened along the Vietnam coast. As clear-sky radiation is practically the same between SS and NS, we attribute the following SWF and LWF effects to differences in the cloud forcing. In the FL–SWO case (Figure 10b), the cooling patch is located over the central South China Sea and its magnitude is up to about −0.15 to −0.2 K after 6 days. While the cloud-forced SWF does not seem to differentially influence the core of the cold tongue between SS and NS, it may be able to extend the width of the cold tongue in the central South China Sea. In contrast, the cloud-forced LWF tends to warm the cold tongue although its impact, as seen in Figure 10c is less than 0.05 K over 6 days, much smaller than that of cloud-forced SWF. The largest impact due to strong monsoon surge is the enhanced latent heat flux over the ocean surface (Figure 10d). The cooling pattern of SST difference between FL and LHO is quite similar to that in Figure 10a except south of 5° N and the core of the cold tongue is effectively cooled (∼−0.4 K over 6 days). On the other hand, the cooling due to the enhanced latent heat flux is comparable with that due to the attenuated shortwave radiation over the central and southern parts of the South China Sea. The enhanced upward latent heat flux is attributed to evaporation triggered by the intense surface wind (e.g., Thompson et al., 2016) associated with strong monsoon surge itself. The upward sensible heat flux is also enhanced and cools down the ocean surface, but its effect is negligible compared with that of the latent heat flux (SHO, Figure 10e).

Figure 11a shows temporal sequences of CT Index, which is defined as the SST averaged over 2°–10° N and 105°–112° E (Koseki et al., 2013; Liu et al., 2004), in the six experiments. Although all of them show a clear diurnal cycle, the longer-term tendency is quite different. Comparing FL with AO, the heat fluxes associated with the strong monsoon surge tend to enhance the cold tongue over the South China Sea (FL) whereas the cold tongue tends to be weakened when there is no surge over the South China Sea (AO). A clear warming tendency can be seen in LHO indicating that the enhanced latent heat flux is essential for strengthening the cold tongue. Although we can see the cooling tendency in SWO, its cooling rate is less than half that of FL. The attenuation

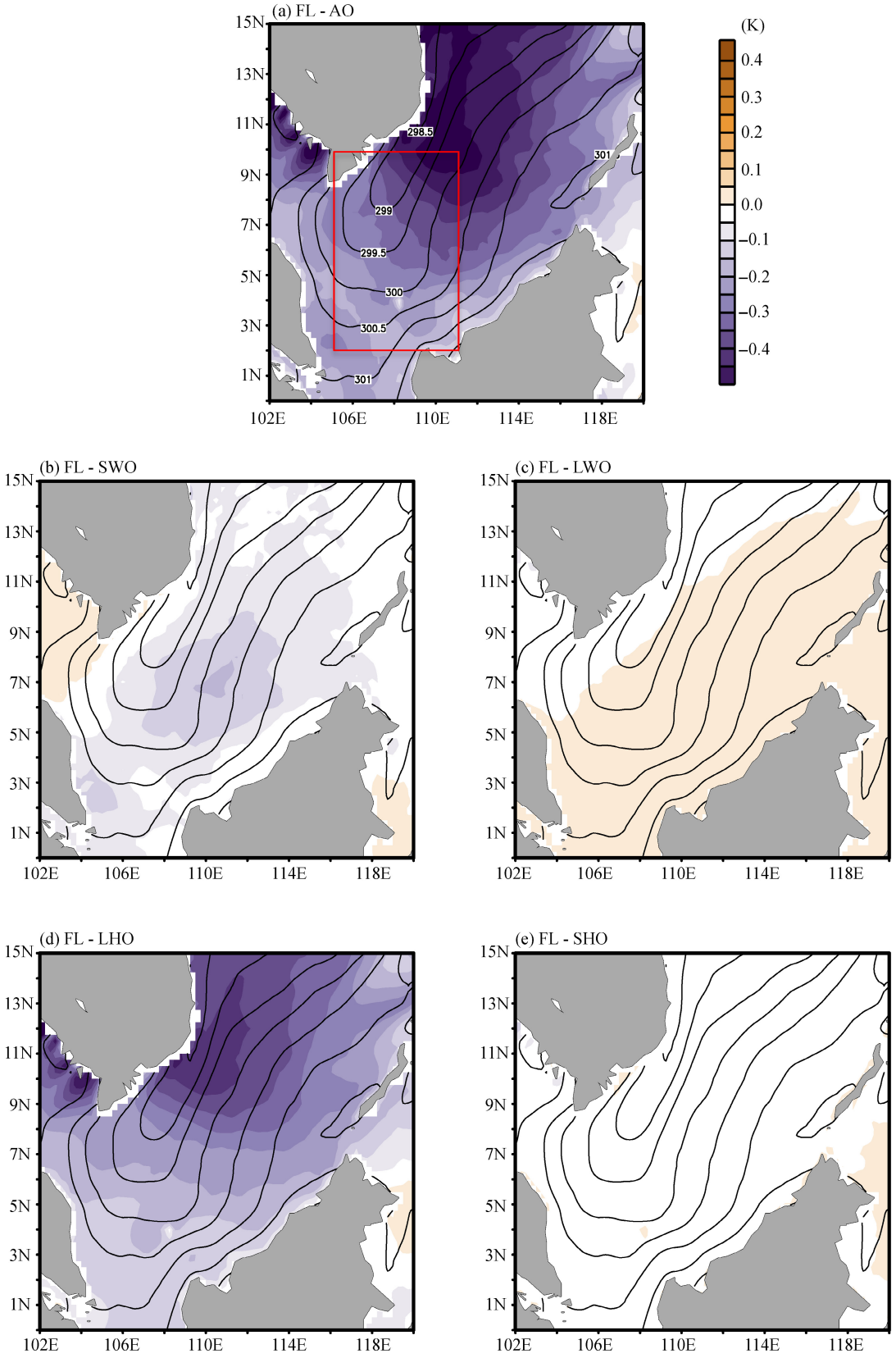

FIGURE 10 The difference in sea surface temperatures (SSTs) (shading; K) after 6 days for the (a) FL-AO, (b) FL-SWO, (c) FL-LWO, (d) FL-LHO, and (e) FL-SHO experiments. The solid contours give the initial SSTs for each experiment, which is set to the OISST 1981–2008 December climatology. The red box in panel (a) is the region used to define the cold tongue (CT) index.

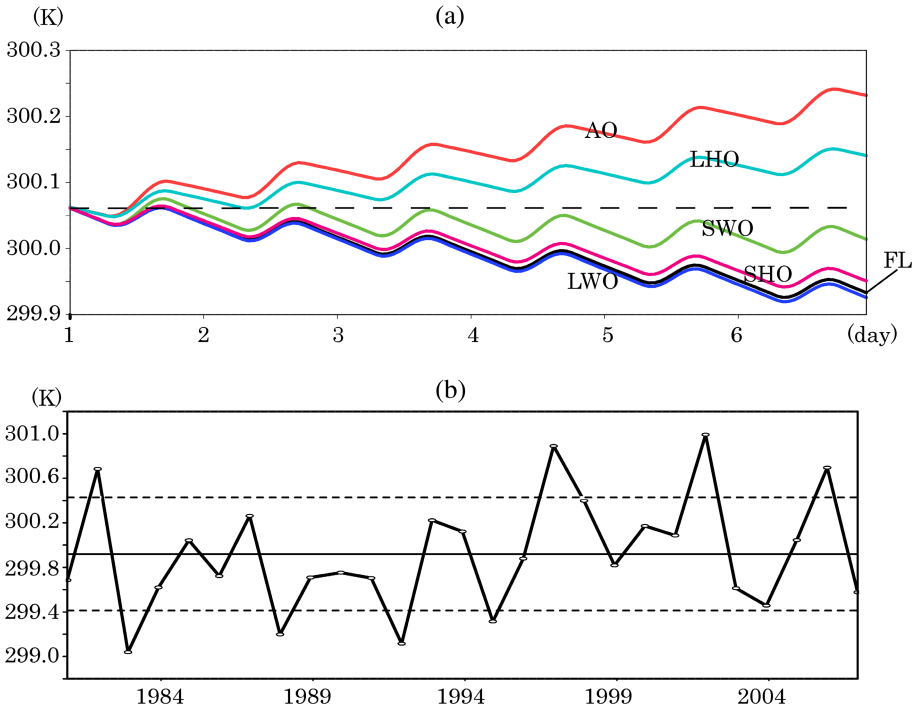

FIGURE 11 (a) Time-series of cold tongue (CT) index, defined as the sea surface temperatures (SSTs) averaged over 2°–10° N and 105°–112° E (red box in a), for each simulation: full flux (black), AO (red), SWO (green), LWO (blue), LHO (cyan) and SHO (magenta). (b) is as (a) but for the 1981–2008 December OISST climatology. The solid (dashed) lines denote the climatology (climatology ± σ) of the CT index.

of SWF by UT clouds clearly plays an important role in enhancing the cold tongue although its contribution is secondary to the enhanced latent heat flux. LWO and SHO do not show much cooling or warming tendencies of the cold tongue consistent with Figure 10.

Generally, the existence of a climatological cold tongue in the South China Sea is induced significantly by the western boundary current along the western coast of Vietnam, which transports cold seawater from higher latitudes equatorward (e.g., Centurioni et al., 2009; Liu et al., 2004). Because our simplified model does not include the components of any ocean dynamics, such as advection, deepening of the mixing layer, and entrainment/detrainment between the mixing layer and thermocline, which are crucial for the SST budget, it will be necessary in the future to explore the full-dynamic processes, including ocean salinity, to understand the heat budget of the cold tongue, as done in Tokinaga and Xie (2011) and Giordani et al. (2013).

7 | CONCLUSIONS

In this study, we have investigated the cloud formation and cloud-radiative forcing associated with strong monsoon surges in the boreal winter monsoon season over the South China Sea using the simulations performed with the WRF model combined with satellite-derived and re-analysis data. The WRF performance was evaluated against that of the CFSR re-analysis, TRMM precipitation and GMS brightness temperature. The model is found to generally reproduce the increased precipitation and associated smaller OLR over the central South China Sea in SS events. This is so despite WRF overestimating the westerly flow to the west of Sumatra and in the Karimata Strait away from the South China Sea. The high-resolution WRF results were subsequently used to investigate the processes behind the upper-level cloud formation in the South China Sea in December.

The upper-level (anvil-type) cloud formation is extensive over the central South China Sea in SS events. As moist cumulus convection is reinforced, the upper-level cloud formation is also enhanced. It exhibits a diurnal cycle that follows the rainfall with a lag of about 5–6 h, which reflects the delay in the larger-scale vertical motion from the lower to upper levels of the troposphere (e.g., Zelinka & Hartmann, 2009). Comparing the diurnal amplitude of OLR between SS and no surge (NS) events, the difference is most remarkable over the central South China Sea. The cloud formation in the whole tropospheric column is reduced in NS with a northward shift of the cumulus convection core (not shown). The UT clouds have a significant impact on the radiation fields: the incoming solar radiation at the surface is attenuated by approximately 80 W m^{-2} over the central South China Sea with slightly enhanced low-level clouds, further reducing the SWF by approximately 10–20 W m^{-2} during SS events. The UT clouds, on the other hand, increase the net downward longwave radiation near the surface by about 15 W m^{-2} in the daily time scale over the central South China Sea.

We conducted a rough estimation of the effects of the attenuated solar radiation on the ocean surface temperature

using a simplified 1D slab ocean model. A series of numerical experiments showed that the enhanced latent heat flux is the largest contributor to the strengthening of the cold tongue in the South China Sea. The shortwave radiation is found to have a secondary impact. The impacts of the sensible heat flux and longwave radiation are negligible. The CT index difference between the AO-FL experiment is about 0.299 K over 6 days (the differences are 0.081, −0.007, 0.208, and 0.018 for SWO, LWO, LHO, and SHO, respectively). This value suggests that a 1-day cold surge event does not seem to have a significant impact on the daily cold tongue temperature tendency. However, the value of 0.299 K over 6 days is equivalent to 60% (LHO, 40%: SWO 16%) of 0.50 K which is one standard deviation of the CT Index as estimated by the OISST December-mean SST from 1981 to 2007 in Figure 11b. Hence, this result indicates that a long-term variation of the cold tongue intensity may be caused partially by the frequency of persistent monsoon surge events mainly through changes primarily in the latent heat flux and secondarily in the UT cloud-forced SWF. Many recent modeling studies show that the diurnal cycle of solar radiation impacts the intraseasonal and mean-state of the tropical SSTs (e.g., Bernie et al., 2005, 2007, 2008; Li et al., 2013; Schiller & Godfrey, 2003; Shinoda & Hendon, 1998). Here, we have shown that the cooling effect due to the monsoon-surge-induced latent heat flux and shortwave radiation may be responsible for long-term maintenance or even enhancement of the cold tongue. According to previous studies (e.g., He & We, 2013; Thompson et al., 2016; Wang & Wu, 2021), the seasonal/interannual variability and development of the SST cold tongue is largely governed by latent heat flux and SWF. In particular, Wang and Wu (2021) suggested that the SST tendency in strong cold tongue years is induced mainly by the latent heat flux and secondarily by the SWF during an anomalously strong East Asian winter monsoon. These results are in line with our findings in this study.

Our study has elucidated that Asian winter monsoon surges influence the upper troposphere over the South China Sea in terms of cloud formation. In particular, the modulation of the radiation budget by ice-phase clouds is prominent, and its impacts can reach downward to the ocean surface and perhaps upward to the Tropical Tropopause Layer. However, one drawback of this study is that the radiation scheme implemented in WRF does not include the interaction between raindrops and radiation, which can also be important. Further numerical experiments in which an ensemble of cloud microphysics and radiation schemes should be considered will be left for future works. In addition, the 1D model used to investigate the role of the different surface radiation and heat fluxes on the ocean heat budget does not account for advection and ocean dynamics, which are known to also play a role in the SST tendency (Wang & Wu, 2021). Experimentation with a coupled model will be presented elsewhere.

AUTHOR CONTRIBUTIONS

Shunya Koseki: Conceptualization (lead); investigation (lead); methodology (supporting); visualization (lead); writing – original draft (lead). **Ricardo Fonseca:** Conceptualization (supporting); formal analysis (supporting); investigation (supporting); methodology (lead); visualization (supporting); writing – original draft (equal); writing – review and editing (equal). **Tieh-Yong Koh:** Conceptualization (supporting); funding acquisition (lead); investigation (equal); methodology (equal); project administration (lead); supervision (lead); writing – original draft (equal); writing – review and editing (equal). **Chee-Kiat Teo:** Formal analysis (supporting); investigation (supporting); methodology (supporting); project administration (supporting); software (lead); supervision (supporting); writing – original draft (supporting); writing – review and editing (supporting).

ACKNOWLEDGEMENTS

We thank the editor and three anonymous reviewers for their comments and suggestions, which have helped to significantly improve the quality of the manuscript. This research was initiated when Shunya Koseki and Chee-Kiat Teo were at the Temasek Laboratories and Ricardo Fonseca and Tieh-Yong Koh were at the Earth Observatory of Singapore (EOS). The authors would like to thank Prof. Jagabandu Panda from the National Institute of Technology Rourkela, India, and Dr. Tengfei Zhang from the EOS for their constructive suggestions on the setting up and execution of the numerical experiments. We are also very grateful to the High Performance Computing Centre at the Nanyang Technological University in Singapore for providing the computational resources needed to perform the numerical simulations presented in this paper. The support of Hwee Jun (Melvin) Soh and Seng Tat (Edwin) Tan is much appreciated. We utilized the versions of 2011Rb and 2013Rb of the MATLAB software package provided by The MathWorks, Inc. (http://www.mathworks.com) and the Grid Analysis and Display System (GrADS; http://www.iges.org/grads/) to manipulate the data and generate the figures.

CONFLICT OF INTEREST STATEMENT

The authors declare that they have no conflicts of interest.

DATA AVAILABILITY STATEMENT

All observational and reanalysis datasets used in this study are available online, and the details of the link are

provided in Table 1. All post-processed WRF simulation data are available upon request from the corresponding author.

ORCID

Shunya Koseki https://orcid.org/0000-0001-7205-7434

REFERENCES

Aldinger, W.T. & Stapler, W. (1998) *Annual tropical cyclone report*. Pearl Harbor, HI: Naval Pacific Meteorology and Oceanography Center/Joint Typhoon Warning Center. Available from: https://apps.dtic.mil/sti/pdfs/ADA381675.pdf [Accessed 20th May 2022].

Bernie, D., Guilyardi, D., Madec, G., Slingo, J. & Woolnough, S. (2007) Impact of resolving the diurnal cycle in an ocean-atmosphere GCM. Part1: a diurnally forced OGCM. *Climate Dynamics*, 29, 575–590. Available from: https://doi.org/10.1007/s00382-007-0249-6

Bernie, D., Guilyardi, D., Madec, D., Slingo, J. & Woolnough, S. (2008) Impact of resolving the diurnal cycle in an ocean-atmosphere GCM. Part2: a diurnally coupled OGCM. *Climate Dynamics*, 31, 909–925. Available from: https://doi.org/10.1007/s00382-008-0429-z

Bernie, D., Woolnough, S., Slingo, J. & Guilyardi, E. (2005) Modeling diurnal and intraseasonal variability of the ocean mixed layer. *Journal of Climate*, 18, 1190–1202. Available from: https://doi.org/10.1175/JCLI3319.1

Centurioni, L.R., Niller, P.N. & Lee, D.-K. (2009) Near-surface circulation in the South China Sea during the winter monsoon. *Geophysical Research Letters*, 36, L06605. Available from: https://doi.org/10.1029/2008GL037076

Chang, C.-P., Liu, C.-H. & Kuo, H.-C. (2003) Typhoon Vamei: an equatorial tropical cyclone formation. *Geophysical Research Letters*, 30, 1150. Available from: https://doi.org/10.1029/2002/GL016365

Charlock, T.P. & Alberta, T.L. (1996) The CERES/ARM/GEWEX experiment (CAGEX) for the retrieval of radiation fluxes with satellite data. *Bulletin of the American Meteorological Society*, 77, 2673–2683.

Chen, J.M., Chang, C.-P. & Li, T. (2003) Annual cycle of the South China Sea surface temperature using NCEP/NCAR reanalysis. *Journal of the Meteorological Society of Japan*, 81, 879–884. Available from: https://doi.org/10.2151/jmsj.81.879

Chen, F. & Dudhia, J. (2001) Coupling an advanced land surface-hydrology model with the Penn State-NCAR MM5 modeling system. Part I: model implementation and sensitivity. *Monthly Weather Review*, 129, 569–585. Available from: https://doi.org/10.1175/1520-0493(2001)129<0569:CAALSH>2.0.CO;2

Chotamonsak, C., Salathe, E.P., Kreasuwan, K., Chantana, S. & Siriwitatakorn, K. (2011) Projected climate change over Southeast Asia using a WRF regional climate model. *Atmospheric Science Letters*, 12, 213–219. Available from: https://doi.org/10.1002/asl.313

Davis, C., Wang, W., Chen, S.S., Chen, Y., Corbosiero, K., DeMaria, M. et al. (2008) Prediction of landfalling hurricanes with the advanced hurricane WRF model. *Monthly Weather Review*, 136, 1990–2005. Available from: https://doi.org/10.1175/2007MWR2085.1

Devabhaktuni, V., Alam, M., Depuru, S.S., Green, R.C., II, Nims, D. & Near, C. (2013) Solar energy: trends and enabling technologies. *Renewable and Sustainable Energy Reviews*, 19, 554–556.

Eguchi, N. & Shiotani, M. (2004) Interseasonal variations of water vapor and cirrus clouds in the tropical upper troposphere. *Journal of Geophysical Research: Atmospheres*, 109, D12106. Available from: https://doi.org/10.1029/2003JD004314

Feng, Z., Dong, X., Xi, B., Schumacher, C., Minnis, P. & Khaiyer, M. (2011) Top-of-atmosphere radiation budget of convective core/staratiform rain and anvil clouds from deep convective systems. *Journal of Geophysical Research*, 116, D23202. Available from: https://doi.org/10.1029/2011JD016451

Fonseca, R., Zhang, T. & Koh, T.-Y. (2016) Improved simulation of precipitation in the tropics using a modified BMJ scheme in WRF model. *Geoscientific Model Development*, 8, 4019–4049. Available from: https://doi.org/10.5194/gmdd-8-4019-2015

Frederick, K. & Schumacher, C. (2008) Anvil characteristics as seen by C-POL during the Tropical Warm Pool International Cloud Experiment (TWP-ICE). *Monthly Weather Review*, 136, 206–222. Available from: https://doi.org/10.1175/2007MWR2068.1

Giordani, H., Caniaux, G. & Voldoire, A. (2013) Intraseasonal mixed-layer heat budget in the equatorial Atlantic during the cold tongue development in 2006. *Journal of Geophysical Research*, 118, 650–671. Available from: https://doi.org/10.1029/2012JC008280

Gu, Y., Liou, K.N., Ou, S.C. & Fovell, R. (2011) Cirrus cloud simulation using WRF with improved radiation parameterization and increased vertical resolution. *Journal of Geophysical Research*, 116, D06119. Available from: https://doi.org/10.1029/2010JD014574

Hattori, M., Mori, S. & Matsumoto, J. (2011) The cross-equatorial northerly surge over the maritime continent and its relationship to precipitation patterns. *Journal of the Meteorological Society of Japan*, 89A, 27–47. Available from: https://doi.org/10.2151/jmsj.2011-A02

He, Z. & We, R. (2013) Coupled seasonal variability in the South China Sea. *Journal of Oceanography*, 69, 57–69. Available from: https://doi.org/10.1007/s10872-012-0157-1

Hong, S.-Y., Noh, Y. & Dudhia, J. (2006) A new vertical diffusion package with an explicit treatment of entrainment process. *Monthly Weather Review*, 134, 2318–2341. Available from: https://doi.org/10.1175/MWR3199.1

Huang, H.J., Liu, H.N., Jiang, W.M., Huang, J. & Mao, W.K. (2011) Characteristic of the boundary layer structure of sea fog on the coast of southern China. *Advances in Atmospheric Sciences*, 28, 1377–1389. Available from: https://doi.org/10.1007/s00376-011-0191-8

Huang, E.Q., Tian, J. & Steinke, S. (2011) Millennial-scale dynamics of the winter cold tongue in the southern South China Sea over the past 26 ka and the East Asian winter monsoon. *Quaternary Research*, 75, 196–204. Available from: https://doi.org/10.1016/j.yqres.2010.08.014

Huffman, G.J., Bolvin, D.T., Nelkin, E.J., Wolff, D.B., Adler, R.F., Gu, G. et al. (2007) The TRMM multisatellite precipitation analysis (TMPA): quasi-global, multiyear, combined-sensor precipitation estimates at fine scales. *Journal of Hydrometeorology*, 8, 38–55. Available from: https://doi.org/10.1175/JHM560.1

Iacono, M.J., Delamere, J.S., Mlawer, E.J., Shephard, M.W., Clough, S. A. & Collins, W.D. (2008) Radiative forcing by long-lived

greenhouse gases: calculation with the AER radiative transfer models. *Journal of Geophysical Research*, 113, D13103. Available from: https://doi.org/10.1029/2008JD009944

Inai, I., Shibata, T., Fujiwara, M., Hasebe, F. & Vömel, H. (2012) High supersatration inside cirrus in well-developed tropical tropopause layer over Indonesia. *Geophysical Research Letters*, 39, L20811. Available from: https://doi.org/10.1029/2012GL053638

Janjić, Z.I. (1994) The step-mountain eta coordinate model: further developments of the convection, viscous sublayer and turbulent closure schemes. *Monthly Weather Review*, 122, 927–945. Available from: https://doi.org/10.1175/1520-0493(1994)122<0927:TSMECM>2.0.CO.2

Joseph, B., Bhatt, B.C., Koh, T.-Y. & Chen, S. (2008) Sea breeze simulation over Malay Peninsula over an intermonsoon period. *Journal of Geophysical Research*, 113, D20122. Available from: https://doi.org/10.1029/2008JD010319

Kahn, B.H., Gettleman, A., Fetzer, E.J., Eldering, A. & Liang, C.K. (2009) Cloudy and clear-sky relative humidity in the upper troposphere observed by the A-train. *Journal of Geophysical Research*, 114, D00H02. Available from: https://doi.org/10.1029/2009JD011738

Klein, S.A. & Hartmann, D.L. (1993) The seasonal cycle of low stratiform clouds. *Journal of Climate*, 6, 1587–1606. Available from: https://doi.org/10.1175/1520-0442(1993)006<1587:TSCOLS>2.0.CO;2

Koseki, S., Koh, T.-Y. & Teo, C.-K. (2013) Effects of the cold tongue in the South China Sea on the monsoon, diurnal cycle and rainfall in the Maritime Continent. *Quarterly Journal of the Royal Meteorological Society*, 139, 1566–1582. Available from: https://doi.org/10.1002/qj2025

Koseki, S., Koh, T.-Y. & Teo, C.-K. (2014) Borneo vortex and mesoscale convective rainfall. *Atmospheric Chemistry and Physics*, 14, 4539–4562. Available from: https://doi.org/10.5194/acp-14-4539

Koseki, S., Nakamura, T., Mitsudera, H. & Wang, Y. (2012) Modeling low-level clouds over the Okhotsk Sea: cloud formation and its effects on the Okhotsk high. *Journal of Geophysical Research*, 117, D05208. Available from: https://doi.org/10.1029/2011JD016462

Koshiro, T. & Shiotani, M. (2014) Relationship between low stratiform cloud amount and estimated inversion strength in the lower troposphere over the global ocean in term of cloud types. *Journal of the Meteorological Society of Japan*, 92, 107–120. Available from: https://doi.org/10.2151/jmsj-2014-107

Lamquin, N., Stubenrauch, C.J. & Pelon, J. (2008) Upper tropospheric humidity and cirrus geometrical and optical thickness: relationships inferred from 1 year of collocated AIRS and CALIPSO data. *Journal of Geophysical Research: Atmospheres*, 113, D00A08. Available from: https://doi.org/10.1029/2008JD010012

Lauer, A., Wang, Y., Phillips, V.T.J., McNaughton, C.S., Bennartz, R. & Clarke, A.D. (2009) Simulating marine boundary layer clouds over the eastern Pacific in a regional climate model with double-moment cloud microphysics. *Journal of Geophysical Research*, 114, D21205. Available from: https://doi.org/10.1029/2009JD012201

Li, Y., Han, W., Shinoda, T., Wang, C., Lien, R.-C., Moum, J.N. et al. (2013) Effects of the diurnal cycle in solar radiation on the tropical Indian Ocean mixed layer variability during wintertime Madden-Julian Oscillations. *Journal of Geophysical Research*, 118, 4945–4964. Available from: https://doi.org/10.1002/jgrc.20395

Lim, K.S.S. & Hong, S.-Y. (2010) Development of an effective double-moment cloud microphysics scheme with prognostic cloud condensation nuclei (CCN) for weather and climate models. *Monthly Weather Review*, 138, 1587–1612. Available from: https://doi.org/10.1175/2009MWR2968.1

Liou, K. (1986) Influence of cirrus clouds on weather and climate processes: a global perspective. *Monthly Weather Review*, 114, 1167–1199. Available from: https://doi.org/10.1175/1520-0493(1986)114<1167:IOCCOW>2.0.CO;2

Liu, Q.Y., Jiang, X., Xie, S.-P. & Liu, W.T. (2004) A gap in the Indo-Pacific warm pool over the South China Sea in boreal winter: seasonal development and interannual variability. *Journal of Geophysical Research*, 109, C07012. Available from: https://doi.org/10.1029/2003JC002179

Mace, G.G., Deng, M., Soden, B. & Zipser, E. (2006) Association of tropical cirrus in the 10-15-km layer with deep convective sources: an observational study combining millimeter radar data and satellite-derived trajectories. *Journal of the Atmospheric Sciences*, 63, 480–503. Available from: https://doi.org/10.1175/JAS3627.1

Miettinen, J., Stibig, H.-J. & Achard, F. (2014) Remote sensing of forest degradation in Southeast Asia: aiming for a regional view through 5-30 m satellite data. *Global Ecology Conservation*, 2, 24–36.

Miller, S.D., Rogers, M.A., Haynes, J.M., Sengupta, M. & Heidinger, A.K. (2018) Short-term solar irradiance forecasting via satellite/model coupling. *Solar Energy*, 168, 102–117.

Monin, A.S. & Obukov, A.M. (1954) Basic laws of turbulent mixing in the ground layer of the atmosphere. *Transanctions of the Geophysical Institute Akademii Nauk USSR*, 151, 163–187.

Norris, J.R. (2005) Trends in upper-level cloud cover and surface divergence over the tropical Indo-Pacific Ocean between 1952 and 1997. *Journal of Geophysical Research: Atmospheres*, 110, D21110. Available from: https://doi.org/10.1029/2005JD006183

Paunas, A.W. & Shanas, S.P. (2017) Atmospheric study of the impact of cold surges and Borneo vortex over western Indonesia Maritime Continent area. *Journal of Climatology & Weather Forecasting*, 5, 189. Available from: https://doi.org/10.4172/2332-2594.1000189

Peng, G., Lemieux, P. & Luquire, K. (2021) Data stewardship maturity report for NOAA daily 0.25° optimum Interpolation Sea surface temperature (OISST) CDR. *National Oceanic and Atmospheric Administration (NOAA) Technical Information Series NESDIS DSMR; 00008*. https://doi.org/10.25923/x3hv-yb57 [Accessed 20th May 2022].

Qian, J.H., Robertson, A.W. & Moron, V. (2010) Interactions among ENSO, the monsoon, and diurnal cycle in rainfall variability over Java, Indonesia. *Journal of the Atmospheric Sciences*, 67, 3509–3524. Available from: https://doi.org/10.1175/2010JAS3348.1

Qu, T. (2001) Role of ocean dynamics in determining the mean state seasonal cycle of the South China Sea surface temperature. *Journal of Geophysical Research*, 106(C4), 6943–6955. Available from: https://doi.org/10.1029/2000JC000479

Reynolds, R.W., Smith, T.M., Liu, C., Chelton, D.B., Casey, K.S. & Schlax, M.G. (2007) Daily high-resolution-blended analyses for

sea surface temperature. *Journal of Climate*, 20, 5473–5496. Available from: https://doi.org/10.1175/2007JCLI824.1

Ricciardulli, L. & Wentz, F.J. (2015) A Scatterometer geophysical model function for climate-quality winds: QuikSCAT Ku-2011. *Journal of Atmospheric and Oceanic Technology*, 32, 1829–1846. Available from: https://doi.org/10.1175/JTECH-D-15-0008.1

Ricciardulli, L., Wentz, F.J. & Smith, D.K. (2011) *Remote sensing system QuikSCAT Ku-2011 monthly ocean vector winds on a 0.25° grid, version 4.* Santa Rosa, CA: Remote Sensing System. Available from: http://www.remss.com/missions/qscat. [Accessed on 10 June 2022].

Rossow, W.B. & Schiller, R.A. (1991) ISCCP cloud data products. *Bulletin of the American Meteorological Society*, 72, 2–20.

Rossow, W.B. & Schiller, R.A. (1999) Advances in understanding cloud from ISCCP. *Bulletin of the American Meteorological Society*, 80, 2261–2288.

Saha, S., Moorthi, S., Pan, H.L., Wu, X., Wang, J., Nadiga, S. et al. (2010) The NCEP climate forecast system reanalysis. *Bulletin of the American Meteorological Society*, 91, 1015–1057. Available from: https://doi.org/10.1175/2010BAMS3001.1

Sakurai, N., Murata, F., Yamanaka, M.D., Mori, S., Hamada, J.I., Hashiguchi, H. et al. (2005) Diurnal cycle of cloud system migration over Sumatera Island. *Journal of the Meteorological Society of Japan Series II*, 83(5), 835–850.

Sandor, B.J., Jensen, E.J., Stone, E.M., Read, W.G., Waters, J.W. & Mergenthaler, J.L. (2000) Upper tropospheric humidity and thin cirrus. *Geophysical Research Letters*, 27, 2645–2648. Available from: https://doi.org/10.1029/1999GL011194

Schiller, A. & Godfrey, J. (2003) Indian Ocean intraseasonal variability in an ocean general circulation model. *Journal of Climate*, 16, 21–39. Available from: https://doi.org/10.1175/1520-0442(2003)016<0021:IOIVIA>2.0.CO;2

Seko, H., Hayashi, S., Kunii, M. & Saito, K. (2008) Structure of the regional heavy rainfall system that occurred in Mumbai, India, on 26 July 2005. *Sola*, 4, 129–132. Available from: https://doi.org/10.2151/sola.2008-033

Shinoda, T. & Hendon, H.H. (1998) Mixed layer modeling of intraseasonal variability in the tropical western Pacific and Indian Oceans. *Journal of Climate*, 11, 2668–2685. Available from: https://doi.org/10.1175/1520-0442(1998)011<2668:MLMOIV>2.0.CO;2

Skamarock, W.C., Klemp, J.B., Dudhia, J., Gill, D.O., Barker, D. M., Wang, W. et al. (2008) A description of the advanced research WRF version 3. NCAR Technical Note TN-468+STR, 113 pp.

Spichtinger, P., Gierens, K., Smit, H.G.J., Ovarlez, J. & Gayet, J.-F. (2004) On the distribution of relative humidity in cirrus clouds. *Atmospheric Chemistry and Physics*, 4, 639–647. Available from: https://doi.org/10.5194/acp-4-639-2004

Steele, C.J., Dorling, S.R., von Glasow, R. & Bacon, J. (2013) Idealized WRF model sensitivity simulations of sea breeze types and their effects on offshore windfields. *Atmospheric Chemistry and Physics*, 13, 443–461. Available from: https://doi.org/10.5194/acp-13-433-2013

Stephens, G.L. (2005) Cloud feedbacks in the climate system: a critical review. *Journal of Climate*, 18, 237–273. Available from: https://doi.org/10.1175/JCLI-3234-1

Stephens, G.L., Vane, D.G., Boain, R.J., Mace, G.G., Sassen, K., Wang, Z. et al. (2002) The CloudSat mission and the A-train. *Bulletin of the American Meteorological Society*, 83, 1771–1790. Available from: https://doi.org/10.1175/BAMS-83-12-1771

Störm, J., Seifert, M., Kärcher, B., Ovarlez, J., Minikin, A., Gayet, J.-F. et al. (2003) Cirrus cloud occurrence as function of ambient relative humidity: a comparison of observations obtained during the INCA experiment. *Atmospheric Chemistry and Physics*, 3, 1807–1816. Available from: https://doi.org/10.5194/acp-3-1807-2003

Thompson, B., Tkalich, P., Malanotte-Rizzoli, P., Fricot, B. & Mas, J. (2016) Dynamical and thermodynamical analysis of the South China Sea winter cold tongue. *Climate Dynamics*, 47, 1629–1646. Available from: https://doi.org/10.1007/s00382-015-2924-3

Tokinaga, H. & Xie, S.-P. (2011) Weakening of the equatorial Atlantic cold tongue over the past six decades. *Nature Geoscience*, 4, 222–226. Available from: https://doi.org/10.1038/NGEO1078

Trilaksono, N.J., Otsuka, S. & Yoden, S. (2012) A time-lagged ensemble simulation on the modulation of precipitation over Western Java in January-February 2007. *Monthly Weather Review*, 140, 601–616. Available from: https://doi.org/10.1175/MWR-D-11-00094.1

Udelhofen, P.M. & Hartmann, D.L. (1995) Influence of tropical cloud systems on the relative humidity in the upper troposphere. *Journal of Geophysical Research*, 100, 7423–7440. Available from: https://doi.org/10.1029/94JD02826

Varikoden, H., Samah, A.A. & Babu, C.A. (2010) The cold tongue in the South China Sea during boreal winter and its interaction with the atmosphere. *Advances in Atmospheric Sciences*, 27, 265–273. Available from: https://doi.org/10.1007/s00376-009-8141-4

Wall, C.J., Hartmann, D.L., Thieman, M.M., Smith, W.L., Jr. & Minnis, P. (2018) The life cycle of anvil clouds and the top-of-atmosphere radiation balance over the tropical West Pacific. *Journal of Climate*, 31, 10059–10080. Available from: https://doi.org/10.1175/JCLI-D-18-18-0154.1

Wang, S., Sobel, A.H., Zhang, F., Sun, Y.Q., Yue, Y. & Zhou, L. (2015) Regional simulation of the October and November MJO events observed during the CINDY/DYNAMO field campaign at gray zone resolution. *Journal of Climate*, 28, 2097–2119.

Wang, Z. & Wu, R. (2021) Individual and combined impacts of ENSO and East Asian winter monsoon on the South China Sea cold tongue intensity. *Climate Dynamics*, 56, 3995–4012. Available from: https://doi.org/10.1007/s00382-021-05682-3

Wang, Y., Xie, S.-P., Xu, H. & Wang, B. (2004) Regional model simulations of marine boundary layer clouds over the Southeast Pacific off South America. Part I: control experiment. *Monthly Weather Review*, 132, 274–296. Available from: https://doi.org/10.1175/1520-10493(2004)132<0274:RMSOMB>2.0.CO;2

Williams, K.D., Ringer, M. & Senior, C. (2003) Evaluating cloud feedback: comparing the response to increased greenhouse gases with current climate variability. *Climate Dynamics*, 20, 705–721. Available from: 10.1007/s00382-002-0303-3.

Zelinka, M.D. & Hartmann, D.L. (2009) Response of humidity and clouds to tropical deep convection. *Journal of Climate*, 22, 2389–2404. Available from: https://doi.org/10.1175/2008JCLI2452.1

Zeng, X. & Beljaars, A. (2005) A prognostic scheme for sea surface skin temperature for modeling and data assimilation. *Geophysical Research Letters*, 32, L14605. Available from: https://doi.org/10.1029/2005GL02303

SUPPORTING INFORMATION

Additional supporting information can be found online in the Supporting Information section at the end of this article.

How to cite this article: Koseki, S., Fonseca, R., Koh, T.-Y., & Teo, C.-K. (2023). Upper tropospheric cloud-radiation interaction induced by monsoon surge over the South China Sea. *Meteorological Applications*, *30*(2), e2125. https://doi.org/10.1002/met.2125